Bioactive Materials 43 (2025) 48–66

Contents lists available at ScienceDirect

Bioactive Materials

journal homepage: www.keaipublishing.com/en/journals/bioactive-materials

Silver-quercetin-loaded honeycomb-like Ti-based interface combats infection-triggered excessive inflammation via specific bactericidal and macrophage reprogramming

Ning Yang [a,1], Ting Wu [b,1], Meng Li [a,1], Xianli Hu [a], Ruixiang Ma [a], Wei Jiang [c], Zheng Su [a,**], Rong Yang [b,***], Chen Zhu [a,*]

[a] Department of Orthopaedics, Centre for Leading Medicine and Advanced Technologies of IHM, The First Affiliated Hospital of USTC, Division of Life Sciences and Medicine, University of Science and Technology of China, Hefei, 230001, Anhui, China
[b] CAS Key Lab for Biomedical Effects of Nanomaterials and Nanosafety, Center of Materials Science and Optoelectronics Engineering, National Center for Nanoscience and Technology, University of Chinese Academy of Sciences, Beijing, 100190, China
[c] Department of Orthopedics, The First Affiliated Hospital of Anhui Medical University, Hefei, Anhui, 230022, China

ARTICLE INFO

Keywords:
Silver nanoparticles
Quercetin
Porous titanium
Macrophage polarization homeostasis
Osteointegration

ABSTRACT

Excessive inflammation caused by bacterial infection is the primary cause of implant failure. Antibiotic treatment often fails to prevent peri-implant infection and may induce unexpected drug resistance. Herein, a non-antibiotic strategy based on the synergy of silver ion release and macrophage reprogramming is proposed for preventing infection and bacteria-induced inflammation suppression by the organic-inorganic hybridization of silver nanoparticle (AgNP) and quercetin (Que) into a polydopamine (PDA)-based coating on the 3D framework of porous titanium (SQPdFT). Once the planktonic bacteria (*e.g., Escherichia coli*, *Staphylococcus aureus*) reach the surface of SQPdFT, released Que disrupts the bacterial membrane. Then, AgNP can penetrate the invading bacterium and kill them, which further inhibits the biofilm formation. Simultaneously, released Que can regulate macrophage polarization homeostasis via the peroxisome proliferators-activated receptors gamma (PPARγ)-mediated nuclear factor kappa-B (NF-κB) pathway, thereby terminating excessive inflammatory responses. These advantages facilitate the adhesion and osteogenic differentiation of bone marrow-derived mesenchymal stem cells (BMSCs), concomitantly suppressing osteoclast maturation, and eventually conferring superior mechanical stability to SQPdFT within the medullary cavity. In summary, owing to its excellent antibacterial effect, immune remodeling function, and pro-osteointegration ability, SQPdFT is a promising protective coating for titanium-based implants used in orthopedic replacement surgery.

1. Introduction

With the increasing prevalence of traumatic fractures, osteoporotic fractures, and degenerative bone and joint disorders, there has been a corresponding rise in the utilization of orthopedic implants. Titanium (Ti)–based metals have emerged as a mainstream choice for orthopedic implants because of their exceptional mechanical properties, biocompatibility, and corrosion resistance [1,2]. Unfortunately, the excellent biocompatibility of Ti-based implants has concurrently resulted in elevated bacterial adhesion. Surface antibacterial modification of implants is a highly effective strategy for preventing peri-implant infections [3]. However, the efficacy of a single antibiotic is limited by its broad-spectrum antibacterial activity [4]. In this context, utilizing silver nanoparticles (AgNPs) is a promising alternative solution because they exhibit broad-spectrum antibacterial activity and potent antibiofilm properties [5,6]. Nevertheless, the application of AgNPs in peri-implant infections is hindered by low bacterial membrane permeability [7]. Excessive Ag nanoparticle usage in turn will cause undesired

Peer review under responsibility of KeAi Communications Co., Ltd.
* Corresponding author.
** Corresponding author.
*** Corresponding author.
E-mail addresses: suz924@ustc.ed.cn (Z. Su), yangr@nanoctr.cn (R. Yang), zhuchena@ustc.edu.cn (C. Zhu).
[1] These authors contributed equally to this work.

https://doi.org/10.1016/j.bioactmat.2024.09.012
Received 4 July 2024; Received in revised form 26 August 2024; Accepted 8 September 2024

cytotoxicity [8,9]. Therefore, how to enhance the safety and specificity of Ag nanoparticles in anti-infective therapy is a key concern that needs to be addressed urgently.

Although current Ti-based implant surface coatings have made some progress in tissue compatibility and antibacterial properties, there is still a lack of a good strategy to simultaneously alleviate peri-implant inflammation and promote osseointegration. This deficiency makes it difficult for Ti-based implants to achieve sufficient stability in the early stages after implantation. Upon bacterial invasion of the human body, the immune system is triggered, thereby initiating a series of inflammatory responses to eradicate infection. It is well known that excessive inflammatory responses can severely disrupt the peri-implant homeostatic balance, resulting in implant failure and poor osseointegration [10]. Implant-bone interface osseointegration is a complex and highly coordinated process that involves the immune microenvironment and bone homeostasis [11,12]. For example, the surface of Ti implants modified with Strontium (Sr) can enhance bone formation by recruiting neutrophils and promoting the secretion of chemokine ligand 12 (CXCL12) [13]. Another study also indicated that activating anti-inflammatory macrophages with Zinc ions can effectively improve bone regeneration on the surface of implants [14,15]. Consequently, the timely modulation of the excessively activated immune microenvironment is crucial for preventing implant failure.

As the most abundant immune cells in the human body, macrophages serve as the primary defense against bacterial pathogens and are a pivotal factor in eradicating inflammatory processes. Quercetin (Que), a flavonoid derived from plants, has been extensively studied for its significant pharmacological impact on various diseases, such as oxidative stress, cancer, nerve injury, inflammation, cardiovascular disease, and obesity [16–18]. The efficacy of Que in diminishing the expression of inflammatory cytokines and reactive oxygen species (ROS) generation in microglial cells, as well as mitigating neuroinflammation, has been demonstrated [19]. Additionally, Que can influence the polarization direction of M1 and M2 macrophages by modulating the Macrophage-inducible C-type lectin (Mincle)/Spleen Tyrosine Kinase (Syk)/Nuclear factor-kappa B (NF-κB) signaling pathway and consequently averting acute kidney injury [20]. Notably, Que also exhibits broad-spectrum antibacterial activity by inhibiting cell wall synthesis, nucleic acid synthesis, and biofilm formation [21–23]. Despite its lower potency compared to antibiotics, Que demonstrates reduced toxicity, fewer side effects, and a lower likelihood of inducing bacterial resistance.

Inspired by mussels, polydopamine (PDA) has been widely used in recent years for the modification of material surfaces due to its strong and universal adhesion and high functional versatility. In this study, we developed a novel PDA-based surface coating on the 3D framework of porous titanium that integrated AgNPs and Que, denoted as SQPdFT. This coating exhibits excellent biosafety and biocompatibility. The 3D-structured surface can further increase the contact area between the implant and the new bone, thereby enhancing the stability of the implant in the medullary cavity through physical means. PDA-based coatings improve the biosafety and biocompatibility of Ti rods. When the planktonic bacteria (*e.g., Escherichia coli*, *Staphylococcus aureus*) touch the surface of SQPdFT, released Que can disrupt the membrane of bacteria to enhance the membrane permeability of AgNP. Then, penetrated AgNPs can kill invading bacteria, which further inhibits biofilm formation. More importantly, incorporating Que terminates infection-induced excessive inflammatory responses by regulating macrophage polarization homeostasis, thereby significantly promoting osseointegration of the implant-bone interface. Through further mechanistic investigations, we elucidated that Que exerted a positive regulatory effect on macrophage polarization homeostasis by activating the peroxisome proliferators-activated receptors gamma (PPARγ)/NF-κB signaling pathway. In conclusion, the PDA-based surface coating loaded with AgNPs and Que is a promising novel strategy for preventing peri-implant infections and excessive inflammatory responses.

2. Methods

2.1. Materials

Medical pure Ti plates (15 mm diameter and 1 mm height) and rods (1 mm diameter and 13 mm height) were purchased from Baoji Shengda Xing Metal Co., Ltd. (Shanxi, China). Tris-HCl buffer (0.01 M, pH = 8.5) was purchased from Leagene Biotechnology Co., Ltd (Beijing, China). $AgNO_3$ was obtained from Alfa Aesar (Shanghai, China). Que and dopamine hydrochloride were acquired from Sigma-Aldrich (Shanghai, China). NaOH, acetone, and ethanol were purchased from Sinopharm Chemical Reagent Co. (Shanghai, China). All reagents were of analytical grade and used without further purification.

2.2. Physicochemical characterization of modified Ti samples

The morphology of the samples was characterized by scanning electron microscopy (SEM, Hitachi S8220). The crystal structure of the samples was determined using X-ray powder diffraction (XRD, Bruker D8 Focus). The sample composition was measured using energy-dispersive X-ray (EDX) analysis. Surface analysis of the sample was performed by X-ray photoelectron spectroscopy (XPS, Thermo Fisher ESCALAB 250Xi). The UV–vis and FTIR absorption spectra of the materials were obtained using a multimode plate reader (Envision, PerkinElmer, America) and a Fourier transform infrared spectrometer (FTIR, spotlight 200i, PerkinElmer, America). The Raman spectra of the materials were obtained using a confocal laser with an excitation wavelength of 514 nm (laser Raman spectrometer, Renishaw inVia plus, Renishaw Company, Britain).

2.3. Sample preparation

(1) Preparation of 3DFT samples: Ti implants were first polished to a mirror surface using different grid sandpapers and ultrasonically cleaned with acetone, absolute ethanol, and deionized water (DI water) for 15 min. After air-drying, Ti samples were placed into 50 mL centrifuge tubes containing 0.2 M NaOH solution in a water bath at 60 °C for 12 h, then cleaned three times with DI water (3DFT samples); (2) Preparation of PDA modified 3DFT (PdFT): PDA was coated on the surface of 3DFT by immersion in 2 mg/mL dopamine solution (0.01 M Tris buffer, pH = 8.5) for 1–24 h under dark conditions. After vigorous washing with DI water and air drying; (3) Fabrication of silver nanoparticles-decorated samples (SPdFT): The PdFT samples were immersed in silver nitrate solution ($AgNO_3$, 10 mg/mL) in an incubator at 37 °C for 12 h. Subsequently, the samples were cleaned three times with DI water and then dried at 50 °C in an air atmosphere; (4) Preparation of Que modified SPdFT samples (SQPdFT): The Que solution with a concentration of 200 μM–10 mM was obtained by dissolving Que in dimethyl sulfoxide and then diluting with ethanol/Tris-HCl buffer solution (2/8, v/v). The SPdFT samples were further dipped into the above obtained Que solution and shaken gently at 37 °C for 12 h. After vacuum drying at 40 °C for 24 h, the SQPdFT samples were finally obtained.

2.4. Bacterial preparation

Escherichia coli (*E. coli*, ATCC 25922), *Staphylococcus aureus* (*S. aureus*, ATCC 6538) and methicillin-resistant *S. aureus* (MRSA, USA300LAC) were cultivated in Luria Broth (LB) medium at 37 °C with 150 rpm rotation for 12 h. The optical density (OD) of each bacterial culture was recorded at 600 nm (*e. g.*, OD_{600} = 0.1, corresponding to a bacterial concentration of 10^8 colony-forming unit (CFU)/mL). After centrifugation at 4000 rpm for 5 min, the LB medium was removed, and the cultures were redispersed in water to a final concentration of 10^7 CFU/mL for future use.

2.5. Morphology examination with SEM

The morphological changes in the bacteria before and after different Ti surface treatments were investigated using SEM. Briefly, after 15 min of incubation with the different samples, the bacteria were fixed with 2.5 % glutaraldehyde for 4 h and gradually dehydrated in a series of ethanol solutions (30 %, 50 %, 60 %, 70 %, 80 %, 90 %, and 100 %, 10 min for each). The as-treated samples were dried and sputtered with Au for 30 s for SEM analysis.

2.6. Establishment of an orthopedic-implant infection model

All animal experiments were approved by the ethics committee of the First Affiliated Hospital of USTC (2023-N(A)-0191).Thirty male Sprague Dawley rats (8 weeks old, mean body weight = 300 ± 50 g) were randomly assigned to six groups based on the type of implant used: control (Ti), Ti (Ti + MRSA), 3DFT (3DFT + MRSA), PdFT (PdFT + MRSA), SPdFT (SPdFT + MRSA), and SQPdFT (SQPdFT + MRSA) (5 rats per group). The animal study protocol was approved by the Animal Ethics Committee of the First Affiliated Hospital of the University of Science and Technology of China (Hefei, China). To establish an implant-associated infection model, we diluted the bacterial solution to a concentration of $1*10^6$ CFU/mL using physiological saline and then spread the diluted bacterial suspension onto various Ti implants (excluding the control group), which were then incubated in a humid atmosphere at 37 °C for 6 h to facilitate bacterial adhesion. Under sterile conditions, Ti rods were implanted into the distal femur. The experimental animals were initially anesthetized using gas under general anesthesia. Following a 10-mm longitudinal incision along the medial side of the knee joint, the extensor mechanism and patella were laterally displaced. The intercondylar fossa was exposed during knee flexion, and a bone canal (1.5 mm in diameter and 15 mm in length) was drilled using an electric drill. Subsequently, the Ti implants were inserted into the bone marrow tube. The patella was then reduced, and the extensor tendon and skin were repaired and sutured. Postoperatively, analgesics were administered to the rats via intramuscular injection daily for one week.

2.7. Cell biocompatibility analysis

Cell viability and cytotoxicity were assessed using the Cell Live/Death staining assay, lactate dehydrogenase (LDH) cytotoxicity assay, and CCK-8 assay to investigate the effects of different coatings on cellular proliferation and toxicity. Briefly, RAW264.7 cells were cultured on different sample surfaces for 48 h and stained with a calcein-AM/PI staining kit (Yeasen, Shanghai, China) to distinguish between viable and non-viable cells. Calcein AM (2 μM) and PI (4.5 μM) were used to label live and dead cells, respectively, and laser confocal microscopy was employed to determine the ratio of live to dead cells. For the LDH cytotoxicity assay, RAW264.7 cells were grown on various Ti plates for 24, 48, and 72 h, and the supernatant was collected following centrifugation. LDH working solution (Beyotime, Shanghai, China) was added to the collected supernatant and incubated for 30 min. LDH activity was determined by measuring the absorbance at 450 nm using a microplate reader. Similarly, for the CCK-8 assay, 10 % CCK-8 solution (Biosharp, Beijing, China) was added to each well of a 24-well plate, and absorbance was measured at a wavelength of 450 nm after incubation for 4 h.

2.8. In vitro antimicrobial activity test

We used the smooth Ti plate group as the control group to study the antibacterial performance of Ti implants with different surface coatings against *S. aureus* and *E. coli*. Cryopreserved strains were first revived at 37 °C on LB and blood agar plates, and colonies exhibiting optimal proliferative activity were selected and inoculated into LB liquid medium using a bacterial inoculation loop. Following a 24-h incubation at 37 °C, the bacterial solution was diluted to a concentration of $1*10^6$ CFU/mL with sterile PBS using a spectrophotometer. Various Ti implants were then infected with the bacterial suspensions and cultured at 37 °C for 6 h. Bacteria (200 μL, $1*10^6$ CFU/mL) were cultured with different samples at 37 °C for 6 h. The bacterial status was visualized using SEM after washing the implants with PBS and briefly fixing, dehydrating, drying, and sputter-coating with gold. To assess bacterial viability in biofilms, the LIVE/DEAD Bacterial Double Stain Kit (Maokang Biotechnology, Shanghai, China) was employed for fluorescence imaging. Red dots represent dead bacteria, while green dots represent live bacteria. A higher proportion of red dots indicates better antibacterial performance of the coating.

To further evaluate the antibacterial efficacy of Ti implants, plate counting was performed. The bacterial suspension was incubated using the same method as in the previous experiment, and ultrasonic elution was used to remove the bacteria from the implant surface after incubation. The washing solution was collected and diluted one thousand-fold with sterile PBS. One day later, 1 mL of bacterial cell suspension was evenly spread on LB agar or blood agar plates and incubated at 37 °C. Each sample was plated multiple times (*e.g.*, three times) to ensure reliable results. After incubation, the colonies on each plate were counted using a colony counter or manually. The antibacterial rate was calculated using the following formula: antibacterial ratio = (A-B)/A*100 %, where A is the average CFU in the Ti control group, and B is the average CFU in the other groups.

The membrane integrity of the bacteria in the various groups was further assessed using O-Nitrophenyl-β-galactoside (ONPG) tests. Bacteria were incubated as previously described, and after adding ONPG solution to the plate, they were cultured for 2 h. The absorbance of the yellow supernatant was measured at 420 nm using a spectrophotometer. When the bacterial membrane was intact, ONPG had difficulty entering the cell, resulting in low endogenous β-galactosidase activity and therefore lower absorbance. When the bacterial membrane was damaged or its permeability increases, ONPG entered the cell and is hydrolyzed to produce ONP, resulting in higher absorbance. Additionally, the bacterial density was semi-quantified using a bacterial ATP test kit (Beyotime, Shanghai, China). After preparing the ATP detection working fluid, the lysate was applied to the wells to lyse bacteria. The working liquid was then added to the wells and allowed to stand for 3–5 min at room temperature. The fluorescence signal of ATP in each group was analyzed using a spectrophotometer, and the ATP concentration in the sample was compared to a standard curve to determine the number of bacteria in the sample. Live bacteria produce and maintain ATP, while dead bacteria do not. Therefore, the higher the survival rate of the bacteria, the stronger the fluorescence intensity; conversely, the higher the mortality rate, the lower the fluorescence intensity.

The antibacterial durability of Ti implants was tested using two approaches. First, the implants were stored in PBS for varying time periods (4, 8, and 12 weeks) before being transferred to 24-well plates, where bacterial suspensions were added to each well and incubated at 37 °C for 24 h. Ultrasonic treatment was used to remove bacteria adhering to the implant surface. The bacterial solution was diluted one thousand-fold with PBS and then plated. Second, the antimicrobial effects of circulating Ti implants were evaluated. Briefly, in each cycle, the sample was submerged in a bacterial solution for 24 h, and then bacteria adhering to the surface of the Ti implants were inoculated onto the plates using ultrasonic treatment. The implants were cleaned for 24 h with 75 % ethanol before being re-tested for antibacterial activity for up to ten cycles.

2.9. In vitro silver ions (Ag^+) release behavior of the coating

The SPdFT and SQPdFT were placed in a 24-well plate and continuously soaked them in 0.5 mL of PBS for 14 consecutive days. We introduced PBS solution samples from days 1, 3, 5, 7, and 14 into the

ICP-MS (iICP-7400, Thermo Scientific) to ascertain the concentration of Ag^+ by spectral analysis.

2.10. In vitro Que release behavior of SQPdFT coating

SQPdFT was placed in a 24-well plate and continuously soaked them in 0.5 ml of PBS for 14 consecutive days. We employed the MicroBCA kit (Sangon, Shanghai, China) to quantify Que content in PBS solution samples collected on days 1, 3, 5, 7, and 14. Initially, Que standards were used to prepare solutions of varying concentrations, which were then added to a 96-well plate along with the test samples. Following the MicroBCA kit instructions, the color reagent was added. The intensity of the color produced by the reaction is directly proportional to the concentration of Que in the sample. The color intensity of the samples was measured using a microplate reader, and the quercetin concentration in the PBS at different time points was calculated based on a standard curve.

2.11. Intracellular AgNPs concentration analysis

S.aureus was respectively released into AgNPs-containing media with or without Que,followed by incubation for varying durations (5 min, 10 min, 15 min, and 20 min). Subsequently, the bacteria adhered to the Ti surfaces were collected and subjected to a triple wash with PBS to eliminate surface-associated AgNPs. The bacteria were then lysed with aqua regia (HNO_3/HCl, volumetric ratio of 1:3) for 2h. Finally, the samples were introduced into an ICP-MS (iICP-7400, Thermo Scientific) to ascertain the concentration of Ag^+ by spectral analysis.

2.12. Macrophage polarization

In this study, RAW264.7 cells were used to investigate the effect of different coatings on macrophage polarization. Cells were seeded at a density of $1*10^5$ per well on the surface of different samples and incubated in 10 % high glucose medium. After 12 h, LPS (100 ng/mL) was added to the wells to mimic the in vivo infection-induced inflammatory microenvironment, and the cells were cultured for 24 h. The expression levels of polarization-related markers were tested using immunofluorescence staining, RT-PCR, and Western blotting. Conditioned media (CM) from all groups was collected and used for subsequent in vitro osteogenic and osteoclast induction experiments.

2.13. Osteogenic differentiation

Primary bone marrow-derived mesenchymal stem cells (BMSCs) were isolated from the femur and tibial shafts of 4-week-old Sprague-Dawley rats using established cell isolation techniques. Upon reaching 90 % confluence, the cells were passaged at a 1:3 ratio and only BMSCs from passages 3 to 6 were used in subsequent osteogenic differentiation assays. To evaluate whether the AgNP-Que hybrid coating can indirectly affect the osteogenic differentiation of BMSCs by regulating macrophage polarization, previously collected CM was mixed with fresh aMEM at a ratio of 1:2 to obtain a new culture medium. β-glycerophosphate (10 mM), dexamethasone (0.1 μM), and ascorbic acid (0.5 mM) were added to the new culture medium for further culture.

The expression levels of the osteogenesis-related genes Alkaline phosphatase (ALP), Bone morphogenetic protein-2 (BMP2), Runt-related Transcription Factor 2 (RUNX2), Osteocalcin (OCN), Osterix (OSX), and Collagen type I alpha 1 chain (COL1A1) were analyzed by RT-PCR one week post-induction, and GAPDH served as the internal reference. All primers were obtained from Sangon Biotech; their sequences are listed in **Appendix** (Supporting information). The detailed PCR procedures have been previously described. ALP staining was also performed using a BCIP/NBT alkaline phosphatase staining kit one-week post-induction. ALP-positive cells were visualized using electron microscopy, and the density of ALP-positive cells per field was calculated to compare osteogenic activity among the groups. Alkaline phosphatase activity was assessed using alkaline phosphatase assay kits (Beyotime, Shanghai, China) and absorbance was measured at 405 nm with a microplate reader. Two weeks post-osteogenic induction of BMSCs, the calcium nodule density in various groups was evaluated using ARS staining. Calcium nodules were dissolved using 5 % perchloric acid, and absorbance of the resulting solution was measured at 490 nm using a microplate reader to semi-quantitatively analyze the mineralization level in each group.

2.14. Osteoclast differentiation

We examined the influence of various Ti implants on osteoclast differentiation using bone marrow-derived macrophages (BMMs). The process of BMMs extraction performed as described in a previous study [24]. The previously collected CM was mixed with fresh DMEM at a ratio of 1:2 to obtain a new culture medium. Then, Receptor Activator of Nuclear factor Kappa-B Ligand (RANKL) (100 ng/mL), MCSF (20 ng/mL), and 10 % fetal bovine serum were added to the new culture medium for further culture. Following one week of osteoclast differentiation induction in BMMs, Tartrate-Resistant Acid Phosphatase (TRAP) staining was performed using a TRAP staining kit (Suzhou Bizhong Biotechnology). The cells were washed three times with PBS and incubated for 30 s with a fixative before being washed with deionized water. The TRAP staining solution was added to the plate and incubated in the dark at room temperature for 30 min. The plates were then washed with deionized water, and the density of TRAP-positive cells per field of view was visualized using electron microscopy. Additionally, the expression of osteoclast differentiation-related genes was analyzed within three days post-induction. The expression levels of TRAP, Nuclear factor-activated T cell 1(NFATc1), Matrix metalloprotein 9 (MMP9), Proto-Oncogene c-fos (c-FOS) and Cathepsin K (CTSK) were detected by RT-PCR, with GAPDH serving as a reference marker. All primers were obtained from Sangon Biotech; their sequences are listed in **Appendix** (Supporting information). The PCR detection procedures have been previously described.

2.15. Western blotting

Following the intervention period, the cells were lysed using (Radioimmunoprecipitation Assay) RIPA lysis buffer, and protein quantification was performed. Proteins were separated by SDS-PAGE gel electrophoresis and transferred from the gel to a PVDF membrane via wet transfer. The PVDF membranes were blocked for 1 h at room temperature with Western blotting blocking solution prior to overnight incubation with primary antibody diluents. After three washes with Tris-Buffered Saline with Tween (TBST), the protein bands were incubated for 1 h at room temperature with the corresponding secondary antibody diluent. Ultimately, target protein expression levels were assessed using Western blot chemiluminescence imaging. All antibodies were obtained from different companies, with detailed information listed in **Appendix** (Supporting information).

2.16. RT-PCR

Total RNA was extracted using Trizol Reagents (Beyotime Biotech, China), and RNA purity and concentration were subsequently assessed using a Nano Photometer spectrophotometer (Thermo Fisher, USA). RNA was reverse-transcribed using a cDNA kit from Monadbiotech (Soochow, China), and real-time PCR was performed using ChemoHS qPCR Mix (Monadbiotech, China). GAPDH was used as an internal control, and mRNA expression levels were quantified using the Light-Cycler 96 SW program.

2.17. RNA sequencing

RAW264.7 cells were stimulated with LPS (100 ng/mL) for 24 h and then treated with Que (20 μM)(Que group) or normal medium (LPS group) for 24 h. Total RNA was isolated using TRIzol reagent (Beyotime), and RNA concentration was assessed using NanoDrop One. Index-coded samples were clustered using the PE Cluster Kit cBot-HS (Illumina) on a cBot Cluster Generation System, according to the manufacturer's instructions. Library preparations were sequenced on the Illumina HiSeq platform, and paired-end reads were generated. Filtered reads were mapped to the Mus musculus genome (GRCm38) using HISAT2, and the number of reads mapped to each gene was counted using HTSeq. Differential expression analysis between two conditions or groups (three biological replicates per condition) was performed using DESeq2 R software. Genes with a P-value less than 0.05 were considered differentially expressed. GO and KEGG pathway enrichment analyses of DEGs were conducted using the hypergeometric distribution method.

2.18. Cell immunofluorescence

After the intervention, the cells were fixed with paraformaldehyde for 20 min and subsequently treated with Triton for 5 min. The cells were then rinsed with PBS and incubated with immunofluorescence-blocking solution at room temperature for 1 h. Primary antibodies were subsequently added, and the cells were incubated for 12 h. Unbound primary antibodies were removed by washing cells with PBS. Fluorescent secondary antibodies and phalloidin were then added and incubated for 1 h. The cells were rinsed again, and a 4′,6-Diamidino-2-Phenylindole (DAPI) staining solution was applied to label the nuclei. Finally, the positive cells were visualized using a fluorescence microscope.

2.19. Immunohistochemistry and tissue immunofluorescence staining

The samples were initially hydrated at room temperature and deparaffinized before undergoing thermal repair using sodium citrate. Endogenous enzyme activity was inhibited using 3 % hydrogen peroxide, and non-specific sites were blocked with goat serum blocking solution. Samples were then coated with primary antibody dilution, placed in a wet box, and refrigerated at 4 °C overnight. After rinsing with PBS, the appropriate secondary antibody was added and incubated for 1 h. Samples were then washed and stained with 3,3′-Diaminobenzidine (DAB) solution by applying 100 μL drop-wise and staining for 3–5 min under a microscope. Hematoxylin counterstaining was performed for 1–2 min, followed by blue staining with 0.5 % ammonia. Samples were then differentiated in 1 % alcohol hydrochloride for 3 s and rinsed for 3 min in tap water before being dehydrated, sealed, and observed under a microscope. For tissue fluorescence staining, samples were incubated with the corresponding fluorescent secondary antibody for 1 h, and the nuclei were subsequently stained with DAPI. The number of positive cells was counted under a microscope.

2.20. Gram staining

The samples were initially outlined using a marking pen and stained with crystal violet for 30 s. The samples were rinsed with distilled water to remove excess dye and then incubated in an iodine solution for 1 min. The samples were then rinsed with distilled water again and decolorized with 95 % alcohol until the purple color was removed. The samples were then incubated with the safranin staining solution for 1 min. Finally, the number of bacteria present was observed under a microscope.

2.21. Histological analysis

Femur samples were immersed in Ethylenediaminetetraacetic acid (EDTA) decalcification solution for four weeks after fixation. The samples were embedded in paraffin and segmented. Histological staining, including H&E, Masson, and TRAP staining, was performed according to the standard protocols described in previous studies. Staining results were visualized under a microscope. H&E staining was used to assess the annulus fibrosus thickness in the medullary cavity and the potential toxicity of Ti implants to vital organs. New bone formation around the bone-implant interface in each group was evaluated using Masson staining. TRAP staining was used to assess the number of osteoclasts within the cancellous bone surrounding Ti implants.

2.22. Micro CT scans

Femur samples were fixed in 4 % paraformaldehyde for 24 h before micro-CT imaging using a SkyScan 1276 (Belgium). Scanning parameters were set to 70 kV, 120 μA, and 200 ms, with a voxel size of 12 μm and medium-mode resolution. Images of various sections of the distal femur were captured using Data Viewer software. Bone structure analysis was performed at the distal end of the femur using CTAn software to define a circular region of interest with a 2 mm radius around the implant. Bone parameters, including bone mineral density (BMD), bone volume (BV), bone surface density (BV/TV), specific bone surface (BS/BV), trabecular thickness (Tb. Th), trabecular number (Tb. N), trabecular separation (Tb. Sp), and connectivity density (Conn.d), were analyzed.

2.23. Biomechanical analysis

Five femurs were randomly selected from each group, and 2 mm of the distal femur was removed to expose the Ti implants. Femurs were then vertically fixed in cement and allowed to dry. Subsequently, the maximum implant fixation strength within the femoral marrow cavity was tested using a material mechanical testing system (Proline; Zwick, Germany). The propulsive velocity was set to 3 mm/min, and the loading force was recorded.

2.24. Statistical analysis

Data analysis was conducted using GraphPad Prism v9, and the results are reported as mean ± SD. For comparisons between two groups, a 2-tailed Student's t-test was used to determine statistical significance, while 1-way or 2-way ANOVA was used for multiple group comparisons. A linear regression F-test was used to evaluate the correlations. Statistical significance was set at $P < 0.05$.

3. Results

3.1. Fabrication and characterization of SQPdFT

A schematic diagram of AgNPs-Que/PDA hybrid coating process is presented in Scheme 1. The scanning electron microscopy (SEM) image in Fig. 1a displays the surface morphology of titanium (Ti) before/after alkali heat treatment and multiple rounds of modification. In contrast to the smooth surface of the untreated Ti plates, the alkali-heat-treated Ti surfaces exhibited a uniform nanoscale honeycomb-like framework structure (denoted as 3DFT). This treatment increased the surface area and porosity of the implant, facilitating the grafting of additional drugs in subsequent modifications. Then, we immersed 3DFT in dopamine solution to uniformly decorate PDA on its surface (denoted as PdFT). Owing to the rich catechol groups on the PDA surface, Ag^{+} could be easily reduced to AgNPs. Therefore, we efficiently modified AgNPs, approximately 25 nm in size, on the surface of PdFT (SPdFT). Finally, to confer additional physiological functionality to the AgNPs/PDA coating, we loaded Que onto its surface (SQPdFT). Que has natural chelating activity due to the catechol portion of its structure that mediates three potential metal binding sites. It can be chelated to metal nanoparticles through electrostatic interactions of catechol groups with metals. An

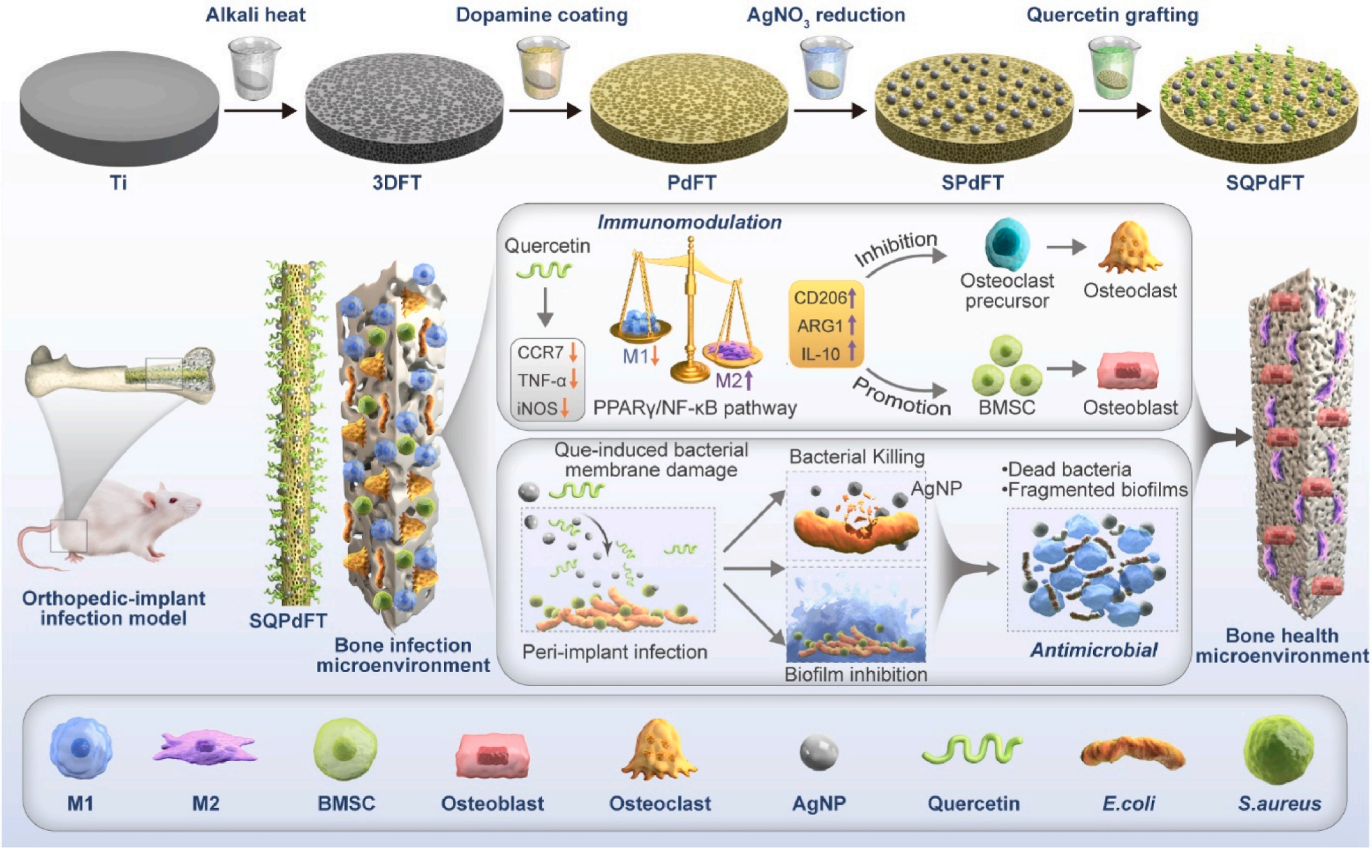

Scheme 1. Schematic illustration of the design, synthesis, and biomedical applications of SQPdFT. SQPdFT is prepared by the organic-inorganic hybridization of AgNPs and Que into a PDA–based coating on the 3D framework of porous titanium. Released Que can disrupt the bacterial membrane of the invading planktonic bacteria. The broken bacterial membrane can elevate the membrane permeability of AgNPs, which can further kill bacteria to inhibit biofilm formation. Importantly, released Que can terminate excessive inflammatory responses via PPARγ/NF-κB pathway-mediated regulation of macrophage polarization homeostasis. In the medullary cavity, SQPdFT has exceptional bone homeostasis repair capacity and superior mechanical stability.

increase in the size of AgNPs modified with Que can also be seen in the SEM image of Fig. 1a. The pore size of the porous Ti surface was about 100 nm; The modification of PDA did not significantly change the pore size, but partially covered the pores; After AgNPs grew on PDA, the NPs homogeneously covered the surface and the pore size was reduced; Finally, after Que modification, the NP sizes changed from ~25 nm to ~40 nm, and surface roughness was increased.

We also investigated the influence of alkali treatment concentration and dopamine immersion time on the drug-loading capacity of the coating. As observed in Fig. S1, a low alkaline concentration resulted in insufficient pore density on the Ti surface, whereas a high alkaline concentration reduced the size of the struts; both scenarios decreased the effective loading area. Clearly, when the NaOH concentration was 0.2 M, the porous surface maintained both good roughness and the highest AgNPs loading, making it the optimal alkaline concentration.

The chemical composition of the AgNPs-Que/PDA hybrid coating was investigated using energy-dispersive X-ray spectrometry (EDS) elemental mapping and X-ray photoelectron spectroscopy (XPS) measurements. First, we verified the uniform distribution of various elements (Ag, C, N, O) on the coating surface (Fig. 1b). The XPS survey spectra in Fig. S2 also revealed that the surface of the AgNPs-Que/PDA hybrid coating displayed peak characteristics corresponding to various elements (Ag, N, C, and O). Fig. S3a showed the N 1s spectrum of the AgNPs-Que/PDA hybrid coating at 400.38 eV, confirming the successful incorporation of dopamine onto the surface [25]. Additionally, O 1s peak at 530.4 eV is attributed to the oxygen in the pyran ring of Que (Fig. S3b) [26]. The C1s peaks of AgNPs-Que/PDA hybrid coating at 284.78, 286.48, and 288.38 eV corresponded to C-C, C-N, and C=O of dopamine and Que, respectively (Fig. S3c) [27]. This signified the effective coverage of the porous Ti surface by the organic layer (PDA and Que). The high-resolution spectrum of Ag (Fig. S3d) showed two peaks and centered at the binding energies of 368.58 and 374.58 eV, attributed to Ag $3d_{5/2}$ and Ag $3d_{3/2}$, respectively [28], due to Ag^{+} reduction to Ag^{0} by PDA with catechol and nitrogen functional groups. The results from UV–vis spectra (Fig. S4) provided additional support for this conclusion. Characteristic surface plasmon resonance (SPR) peaks of AgNPs were observed at λ_{max} = 400–500 nm [29]. Neither dopamine nor $AgNO_3$ solutions exhibited distinct absorbance peaks. However, a mixed solution of dopamine and $AgNO_3$ displayed a strong absorption peak at 450 nm, confirming the reduction of Ag^{+} in the solution to Ag^{0}, forming AgNPs.

The water contact angle (WCA) values of Ti, 3DFT, PdFT, SPdFT, and SQPdFT are presented in Fig. 1c. The introduction of nanopores reduced the implant's WCA value from 78 ± 0.5° to 11.5 ± 1.3°. Subsequent modification with PDA, AgNPs, and Que increased the scaffold's WCA values to 24.17 ± 1.15°, 32.5 ± 0.5°, and 55.5 ± 0.5°, respectively. These results indicated that the hydrophilicity of the Ti implant was changed through the successive introduction of a nanoporous network and surface modifications with PDA, AgNPs, and Que. This phenomenon can be attributed to bioactive -OH and $-NH_2$ groups in PDA and Que [30, 31].

Due to the overlap of the X-ray diffraction (XRD) peaks of Ti (JCPDS no. 44–1294) at 38.421 (002) and 40.170 (101), as well as Ag (JCPDS no. 41–1402) at 35.891 (004) and 40.301 (112) (Fig. 1d), we conducted additional surface structure analyses using Raman and FTIR spectroscopy. AgNPs exhibit surface-enhanced Raman scattering (SERS)

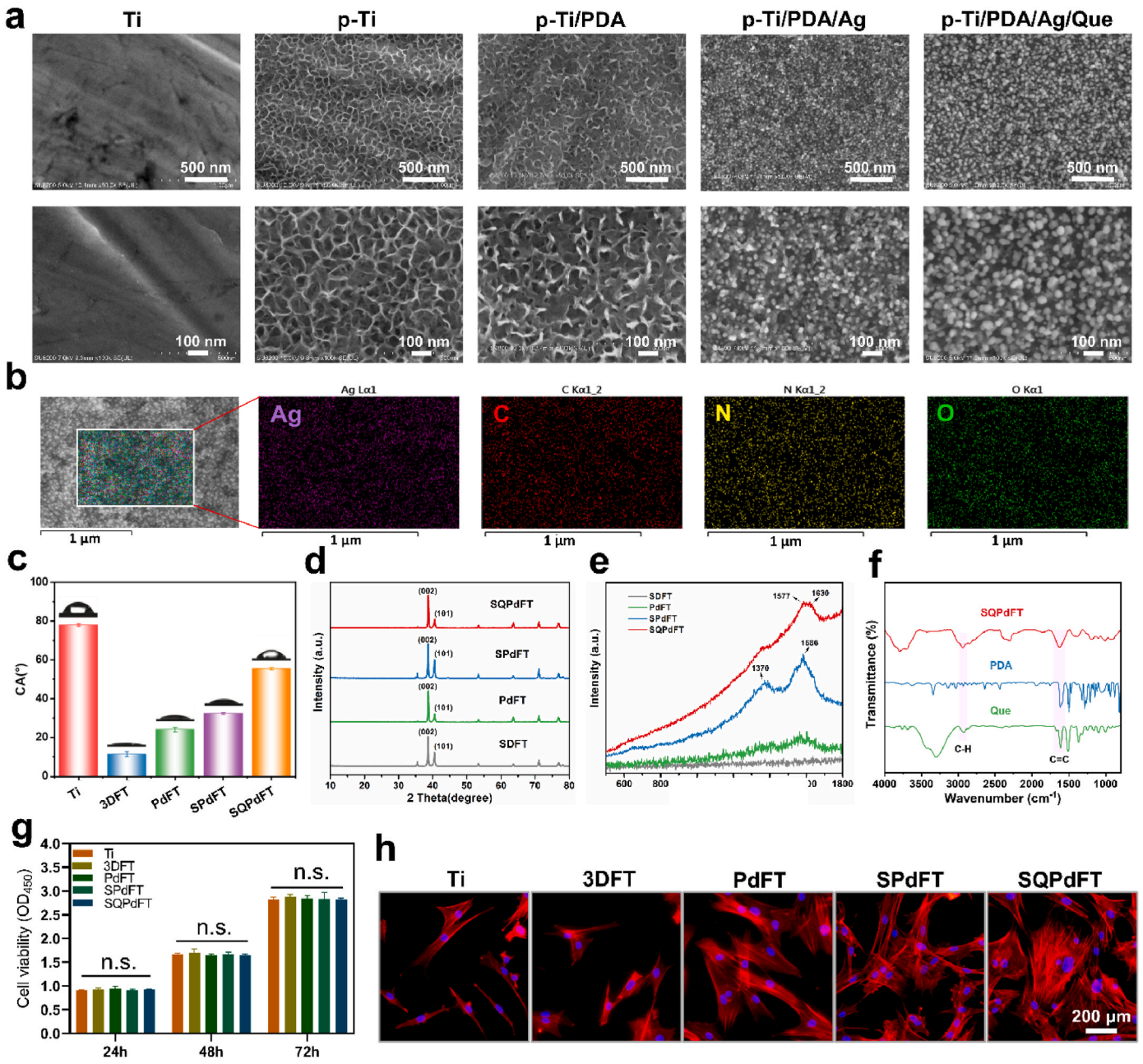

Fig. 1. Physicochemical characterization and biocompatibility assessment of the SQPdFT surfaces. (a) SEM images showing the surface morphology of Ti, 3DFT, PdFT, SPdFT, and SQPdFT. Scale bar: 500 nm and 100 nm, respectively. (b) EDS elemental mapping (Ag, O, C, and N) images of the SQPdFT surfaces. Scale bar: 1 μm. (c) Contact angles of the various surfaces. (d) XRD patterns of 3DFT, PdFT, SPdFT, and SQPdFT. (e) Raman shifts for 3DFT, PdFT, SPdFT, and SQPdFT. (f) FTIR spectra of PDA, Que, and SQPdFT. (g) Cell viability of RAW264.7 cells cultured on different Ti plates for 24, 48, and 72 h. Data represents the means ± S.D. (n = 5 per group). n.s. indicates no significance. (h) CLSM images of BMSCs adhered onto the different Ti sheet's surfaces. Scale bar: 200 μm, respectively.

properties, and the size and shape of these nanoparticles significantly influence the SERS characteristics of the material surface [32]. Fig. 1e of the Raman spectra revealed a broad peak on the PdFT surface in the range of 1300–1600 cm^{-1}, with a weak peak intensity. This peak arises from the stretching vibration (1370 cm^{-1}) and deformation vibration (1586 cm^{-1}) of the benzene ring within the polydopamine structure [33]. The intensities of the peaks at 1370 cm^{-1} and 1586 cm^{-1} on the Ti surface were enhanced by loaded AgNPs. With Que modification, the region between 1577 and 1630 cm^{-1} could also be attributed to C=O and C=C vibrations of Que [34]. The FTIR spectrum of AgNPs-Que/PDA hybrid coating exhibited pronounced and broad absorption bands in the range of 1750-750 cm^{-1}, corresponding to the OH bending of phenols, C−CO−C stretching and bending in the ketone band, C=O of the C ring, and aromatic out-of-plane C−H bending vibrations attributable only to Que [35]. The peak at 2935 cm^{-1} corresponded to the aliphatic C−H stretching of CH_2 [36], and the peak at 1622 cm^{-1} could be attributed to the overlap of the C=C resonance vibration in the aromatic ring. The regions corresponding to C−C, C−O, and C−N were within the range of 1200–1500 cm^{-1} [37]. These characteristics closely resembled those observed in the spectra of pure PDA and Que (Fig. 1f). These findings confirmed the successful preparation of AgNPs and Que coating on the porous Ti surface.

3.2. Biocompatibility assessment

The foremost objective of surface modification of Ti implants is to

endow them with excellent cellular compatibility. In fact, free AgNPs tend to specifically distribute in organs such as the lungs, kidneys, liver, and spleen, while depositing less in bone tissue [38]. However, considering that the explosive release of Ag^+ can still induce local cell apoptosis [39,40], we first examined the Ag^+ release characteristics of SPdFT and SQPdFT. The results showed that both SPdFT and SQPdFT maintained a slow and steady release of Ag^+ over a period of up to 14 days (Fig. S5). The release rate of Ag^+ from SQPdFT was slower, which may be attributed to Que containing multiple hydroxyl and keto groups that form chelates with Ag^+, thereby slowing down the release of Ag^+. Then, we conducted preliminary assessments of the cytotoxicity of AgNPs/PDA and AgNPs-Que/PDA hybrid coatings through cell viability staining experiments. We found that SPdFT, and SQPdFT did not increase cell death compared to the Ti group (Fig. S6). The LDH and CCK8 assays also revealed that SPdFT, and SQPdFT had no significant impact on RAW264.7 cell proliferation, indicating firm anchoring of AgNPs on the surface of the coating (Fig. S7 and Fig. 1g). This is consistent with previous research findings, indicating that AgNPs have a strong anchoring effect on PDA-based coating surfaces and exhibit good biosafety [41,42]. Next, we observed the adhesion morphology of BMSCs on the various sample surfaces. The SEM images showed that the BMSC spreading area on the porous Ti and PdFT surfaces was significantly larger than that on the unmodified Ti surfaces (Fig. S8). Although there was Ag^+ release, we did not observe any morphological changes in BMSCs on the SPdFT surface. This further indicates that the Ag^+ concentration released from the SPdFT coating is within a safe range. Interestingly, the BMSCs in the SQPdFT group exhibited the most filopodia and lamellipodia. CLSM images also showed that BMSCs on the AgNPs-Que-coated surfaces had more abundant cell extensions compared to the SPdFT group, further confirming the excellent cell adhesion of this coating (Fig. 1h). According to the literature, even at a low concentration of 1 μM in solution, Que can promote the osteogenic differentiation of BMSCs, regulate M1/M2 macrophage polarization, and maintain oxidative/antioxidant balance [43,44]. After soaking our SQPdFT coating in PBS for 24 h, the concentration of Que reached 2.11 μM (Fig. S9). This concentration of Que is sufficient to produce the biological effects observed in our aforementioned experimental results. A recent study also supports our observation, in which they found that Que-modified Ti6Al4V implants effectively promote the adhesion and osteogenic differentiation of BMSCs [45]. Overall, these results suggest that the dual-modified AgNPs-Que/PDA hybrid coating significantly improves Ti implant biocompatibility, which is highly favorable for peri-implant bone reconstruction.

3.3. High bactericidal activity and mechanism investigation

Despite the remarkable bactericidal efficacy of AgNPs against various bacteria, including drug-resistant strains, they have not yet provided a comprehensive solution for the challenge of bacterial drug resistance. Bacteria tend to develop resistance to Ag^+ after prolonged exposure to sublethal concentrations of Ag^+ [46–48]. Both *E. coli* and *S. aureus* can synthesize pyridine, thus reducing the bioavailability of silver by detoxifying Ag^+ to Ag^0 [49]. As an antibacterial strategy, multidrug combination therapy has some unparalleled advantages, including enhanced antimicrobial efficacy, resistance to bacterial drug resistance, and a broader spectrum of antimicrobial effects [50,51]. Several previous studies have confirmed that when Que is used in combination with antibiotics, it demonstrates a strong synergistic effect, significantly enhancing their antibacterial activity [50,52]. Therefore, we postulate that Que inclusion further augments the antibacterial performance of the coating. Considering that *E. coli* and *S. aureus* are the two main pathogenic bacteria causing orthopedic peri-implant infections, we first assessed the sterilization efficacy of different samples against *E. coli* and *S. aureus* adhering to the surfaces via CFU plate counting. As shown in Fig. 2a and b, the number of bacterial colonies remaining on the surfaces of SPdFT and SQPdFT is significantly lower than that in other groups, demonstrating notable antibacterial activity. Quantitative analysis revealed that SPdFT exhibited antibacterial effects of 83.6 % against *S. aureus* and 75.6 % against *E. coli*. As expected, the incorporation of Que further enhanced the antibacterial activity of SQPdFT, achieving antibacterial effects of 96.3 % against *S. aureus* and 97.7 % against *E. coli*. We also observed the morphology of *S. aureus* and *E. coli* on different implant surfaces using scanning electron microscopy. Consistent with the results mentioned above, the number of bacterial colonies on the SQPdFT surface was significantly lower than that on other sample surfaces. Furthermore, the bacteria on the SQPdFT surface exhibited shrinkage and were smaller in size compared to those in other groups (Fig. 2c).

Numerous literatures have shown that the primary mechanisms by which Que inhibits the growth of various types of bacteria are through disrupting cell membranes and altering membrane permeability [53–55]. It has been reported that at concentrations of 10–50*MIC, Que can cause cell wall lysis and leakage of intracellular substances in *S. aureus* and *E. coli* [53]. The core mechanism may be that Que alters the structure of bacterial cell membranes by increasing the conductivity of the bacterial solution [56]. Next, we assessed the impact of Que on the intracellular concentration of AgNPs in *S. aureus*. The inductively coupled plasma-mass spectrometry (ICP-MS) analysis results revealed that, under Que intervention, the enrichment levels of AgNPs were significantly higher than the baseline, indicating that the augmented antimicrobial efficacy of SQPdFT can be primarily ascribed to the elevation of bacterial cell membrane permeability facilitated by Que (Fig. 2d). It is well known that damage to bacterial walls and cell membranes can result in abnormal energy metabolism within bacteria [57]. The Adenosine 5′-triphosphate (ATP) intensity in each group was assessed using an ATP assay kit. Compared to the Ti group, the SQPdFT group exhibited the most pronounced reduction in ATP intensity (~96.7 %), while the ATP density in the SPdFT group only decreased by 87 % (Fig. 2e). This suggested a pronounced synergy between Que and AgNPs, causing severe disruption of bacterial cell membranes. ONPG can readily penetrate bacterial membranes and react with the intracellular enzyme β-D-galactosidase to produce yellow-nitrophenol. The results of the ONPG assay also indicated that the SQPdFT group showed the highest β-galactosidase activity, reconfirming that the antibacterial effects of SQPdFT on *S. aureus* and *E. coli* were attributable to bacterial membrane damage (Fig. 2f).

Biofilm formation is a critical factor for bacterial immune evasion and resistance [58,59]. Therefore, preventing bacterial colonization and biofilm formation is essential for avoiding peri-implant infections. We comprehensively evaluated the biofilm resistance of various samples using SYTO9/PI fluorescence staining assays. Fluorescence images revealed that Ti, 3DFT, and PdFT surfaces were entirely covered with green fluorescence, indicating intact biofilms on their surfaces. In contrast, biofilm coverage on the surfaces of SPdFT and SQPdFT was significantly reduced. Among them, the SQPdFT surface exhibited the smallest area of green fluorescence and the highest biofilm resistance (Fig. 2g). Furthermore, compared with the control group, the SQPdFT surface exhibited numerous red fluorescence spots, indicating bacterial death and biofilm disruption. Excitingly, we found that SQPdFT also exhibited strong antibacterial effects against MRSA (Fig. S10), further confirming the broad-spectrum antibacterial properties of our coating.

Typically, the osseointegration interface around the implant takes at least three months to fully form [60]. Therefore, whether SQPdFT has long-lasting antibacterial properties is another important issue that must be considered. Using the antibacterial effect against *S. aureus* as an example, although the antimicrobial rate of SQPdFT decreased with increased PBS immersion time, it remained at 82.4 % by the 12th week (Fig. 2h). More convincingly, in the cycle antibacterial experiments, we found that the antimicrobial rate of SQPdFT remained at 86.7 %, even at cycle 10 (Fig. 2i). These results demonstrate that our SQPdFT retained its antimicrobial properties and provided antibacterial protection during the entire peri-implant new bone formation process. This may be

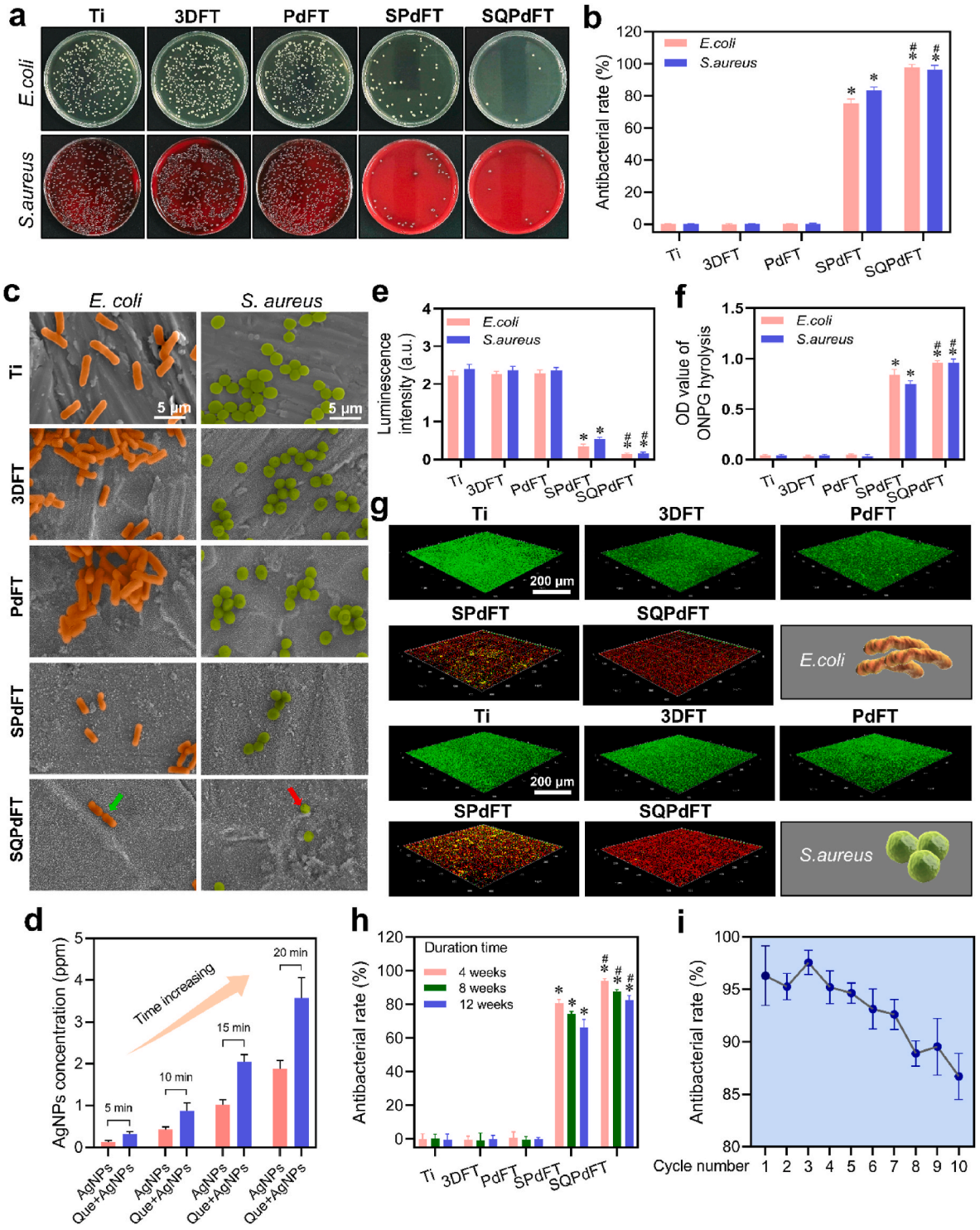

Fig. 2. Antibacterial properties of Ag and Que co-modified porous Ti surfaces. (a) Solid culture after incubating *E. coli* and *S. aureus* (10^6 per mL) on various Ti sheet surfaces for 24 h. (b) The antibacterial efficacy of diverse implant materials was assessed by enumerating bacterial colonies. Data represent mean ± S.D. (n = 3 per group). (c) SEM images of *E. coli* and *S. aureus* cultured on various Ti plates, disrupted cells were indicated by red arrows. Scale bar: 5 μm. (d) ICP-MS analysis of intracellular AgNP concentration. (n = 3 per group). (e) The ATP production levels in bacteria were quantified using an ATP Assay Kit. Data represent mean ± S.D. (n = 5 per group). (f) The ONPG hydrolysis assay results. Data represent mean ± S.D. (n = 5 per group). (g) CLSM images of biofilms of *E. coli* and *S. aureus* cultured on various Ti sheet surfaces. Red (Dead bacteria), green (Live bacteria). Scale bar: 200 μm. (h) Quantitative analysis of the long-lasting antibacterial efficacy of different implants stored in PBS for varying durations using CFU counting. Data represent mean ± S.D. (n = 3 per group). (i) Quantitative analysis of the repeated antibacterial efficacy of SQPdFT using CFU counting. Data represent mean ± S.D. (n = 3 per group). * indicates a statistical difference compared to the Ti group ($P < 0.05$) and # indicates a statistical difference compared to the SPdFT group ($P < 0.05$).

attributed to creating a surface on the Ti implant with a high porosity and surface area, thereby increasing the loading of AgNPs and Que. On the other hand, the PDA-based coating effectively enhanced the anchoring of AgNPs, preventing the rapid loss of antibacterial effectiveness due to Ag^{+} detachment.

3.4. M1 to M2 phenotypic transition of macrophage by SQPdFT

Peri-implant inflammation can seriously harm osseointegration, particularly when it is caused by infection [61,62]. In fact, in the microenvironment of peri-implant infection, macrophages are not only immune phagocytic cells but also key regulators of bone homeostasis [63]. To expedite peri-implant osseointegration, it is imperative to promptly shift macrophages from a proinflammatory phenotype (M1) to an anti-inflammatory phenotype (M2). Therefore, to confirm the anti-inflammatory properties of SQPdFT, we investigated its influence on macrophage phenotypes. First, we examined the polarization direction of the macrophages to investigate the immunomodulatory capabilities of various samples. We induced RAW264.7 cells toward M1 polarization by adding LPS to the culture medium to mimic the inflammatory microenvironment induced by bacterial infections. Cells grown on the smooth Ti plates without any treatment were used as control. From the immunofluorescence assay results, we observed a significant increase in ARG1 (M2 marker) expression in the SQPdFT group compared to that in the Ti group, while the expression of iNOS (M1 marker) decreased (Fig. 3a–c). We further quantified the protein and gene levels of M1 polarization-related markers (iNOS and CD86) and M2 polarization-related markers (CD163 and CD206) using WB and

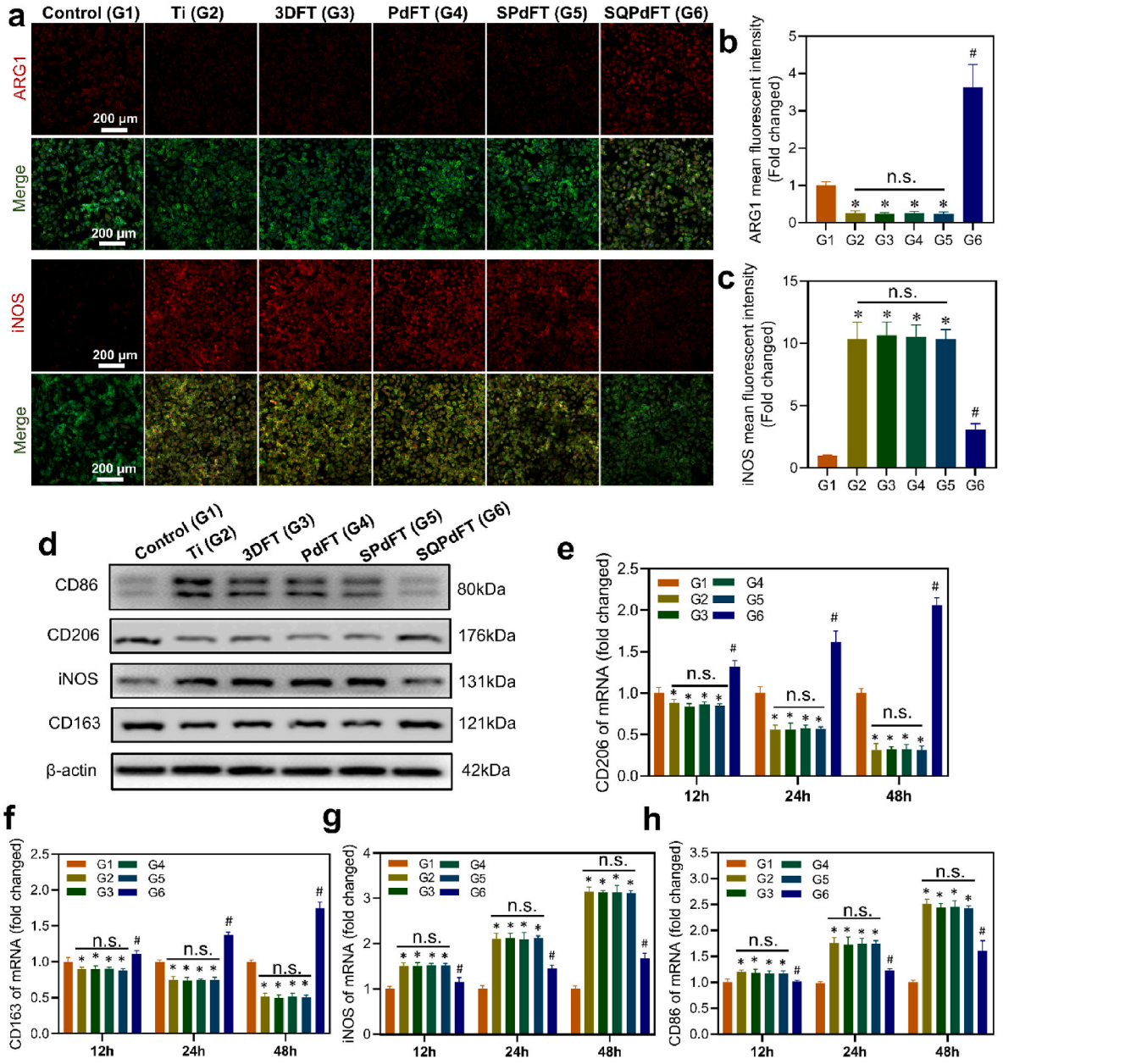

Fig. 3. SQPdFT regulates macrophage polarization homeostasis. (a) CLSM images of ARG1-positive and iNOS-positive RAW264.7 cells. Scale bar: 200 μm. (b, c) The mean fluorescence intensities of ARG1 and iNOS were measured by Image J. Data represent the means ± S.D. (n = 3 per group). (d) Western blot analyses of the levels of macrophage polarization related-markers protein expression. (e–h) Relative mRNA expression of macrophage polarization-related markers in RAW264.7 cells. Data represents the means ± S.D. (n = 3 per group). n.s. indicates no significance, * indicates a statistical difference compared to the control group ($P < 0.05$) and # indicates a statistical difference compared to the Ti group ($P < 0.05$).

RT-PCR assays. Consistent with the immunofluorescence assay results, the SQPdFT group exhibited the lowest levels of iNOS and CD86 expression and the highest levels of CD163 and CD206 expression, except for the control group. In contrast, SPdFT did not have a detectable effect on the expression of polarization-related markers (Fig. 3d–h and Fig. S11). These findings provide compelling evidence that SQPdFT can facilitate polarization from M1 to M2 in macrophages, which is manipulated by Que.

3.5. Regulatory mechanisms of macrophage polarization homeostasis

To gain insights into the immunoregulatory mechanism of Que in macrophages, we performed a transcriptome analysis on RAW264.7 cells treated with LPS (LPS group) or Que + LPS (Que group). Principal component analysis (PCA) indicated significant clustering of mRNA in LPS and Que + LPS-treated cells (Fig. 4a). We identified 3380 differentially expressed genes, with 1484 upregulated and 1896 downregulated in response to Que intervention (Fig. 4b). Notably, compared to the LPS group, a multitude of genes associated with inflammation and M1 polarization were downregulated in the LPS + Que group, while anti-inflammatory genes and M2 polarization-related markers were upregulated (Fig. 4c). Gene ontology (GO) enrichment analysis revealed that eight of the top ten processes with lower expression after Que treatment were related to inflammatory reactions (Fig. 4d). The NF-κB signaling pathway plays a dual role in the infection process, governing both the secretion of inflammatory factors and the phenotypic regulation of macrophages [64,65]. Que can ameliorate the inflammatory microenvironment by inhibiting the NF-κB pathway [66]. Our KEGG enrichment analysis results and gene set enrichment analysis (GSEA) results revealed that, following Que intervention, the activities of inflammation-related pathways such as NF-κB signaling, TNF signaling, and IL-17 signaling pathways were significantly downregulated, whereas the peroxisome proliferator-activated receptor (PPAR) pathway was upregulated (Fig. 4e–g).

PPARs are a family of transcription factors activated by fatty acids and are expressed in adipose tissue and immune cells [67,68]. Numerous studies have proven that there is crosstalk between PPARγ and inflammatory responses [69,70]. PPARγ inhibits M1 polarization and reduces proinflammatory responses by binding to P65 or inhibiting P65 acetylation [71]. Knocking out PPARγ selectively in bone marrow-derived macrophages (BMMs) in mice reduces M2 marker activity [72]. It has been reported that Que can promote macrophage M2 polarization and improve ulcerative colitis by regulating STAT1 to activate PPARγ [73]. Furthermore, another study has shown that Que can also inhibit the expression of the MAPK pathway in RAW264.7 cells [74]. It is well-known that in inflammatory responses, activation of the MAPK pathway can promote the expression of inflammatory factors by inhibiting PPARγ expression and activity [75,76]. Therefore, PPARγ may be a key factor in Que-mediated regulation of macrophage polarization. However, whether PPARγ functionally participates in Que-mediated regulation of the NF-κB pathway remains unclear. To validate our hypothesis, we first examined the regulatory effect of Que on the expression of PPARγ and NF-κB pathway-related proteins. As presented in Fig. 4h–m, LPS activated the NF-κB pathway and downregulated PPARγ expression. However, Que intervention not only inhibited the phosphorylation of P65 and degradation of IκBα but also reversed the LPS-induced inactivation of PPARγ. This suggests that PPARγ may play a role in Que-mediated modulation of the NF-κB signaling pathway. To further investigate whether PPARγ activation was positively correlated with Que's promotion of M2 macrophage polarization, we introduced a PPARγ inhibitor, Mifobate, into the culture medium of the LPS + Que group. We observed a dose-dependent increase in the expression of M1-related markers and a decrease in the expression of M2-related markers following Mifobate treatment (Fig. 5a–e). Immunofluorescence analysis results were consistent with those of Western blot analysis, showing that mifepristone nearly completely counteracted the effect of Que on macrophage polarization (Fig. 5f). In conclusion, these findings support our hypothesis that Que directly regulates macrophage polarization equilibrium through the PPARγ/NF-κB pathway, thereby reshaping the inflammatory microenvironment (Fig. 5g).

3.6. Immunomodulation-mediated bone homeostasis repair in vitro

We utilized a macrophage-CM to further investigate whether the immunomodulatory effects of SQPdFT impact the osteoclastogenesis of bone marrow macrophages (BMM) and osteogenic differentiation of BMSCs. Bone marrow macrophages were cultured in osteoclastogenic medium supplemented with CM^{Ti}, $CM^{Ti + LPS}$, $CM^{3DFT + LPS}$, $CM^{PdFT + LPS}$, $CM^{SPdFT + LPS}$ or $CM^{SQPdFT + LPS}$ for six days (Fig. 5h). TRAP staining clearly demonstrated a significant reduction in osteoclast formation induced by $CM^{SQPdFT + LPS}$ compared to that in the $CM^{Ti + LPS}$, $CM^{3DFT + LPS}$, $CM^{PdFT + LPS}$ and $CM^{SPdFT + LPS}$ groups (Fig. 5i and Fig. S12a). Furthermore, RT-PCR results indicated that CM^{SQPdFT} reduced the expression of osteoclast differentiation-related genes (NFATc1, MMP9, c-FOS, TRAP, and CTSK) (Figs. S12b–f). We then treated the BMSCs using the same procedures (Fig. 5j). ALP staining results showed that ALP activity in the $CM^{Ti + LPS}$, $CM^{3DFT + LPS}$, $CM^{PdFT + LPS}$, and $CM^{SPdFT + LPS}$ groups was significantly lower than that in the CM^{Ti} group (Fig. 5k and l). In contrast, $CM^{SQPdFT + LPS}$ only mildly reduced ALP activity. Additionally, Alizarin Red S (ARS) staining further confirmed that the calcium deposition levels in the $CM^{SQPdFT + LPS}$ group were 10.1-fold, 9.5-fold, 10.1-fold, and 10.51-fold higher than those in the $CM^{Ti + LPS}$, $CM^{3DFT + LPS}$, $CM^{PdFT + LPS}$, and $CM^{SPdFT + LPS}$ groups, respectively, consistent with the control group (Fig. 5k and m). The expression levels of six osteogenic differentiation-related genes (BMP2, RUNX2, OCN, ALP, OSX, and COL1A1) exhibited similar trends (Figs. S13a–f). These findings provide strong evidence that SQPdFT can promote bone homeostasis repair by modulating the immune microenvironment.

3.7. In vivo anti-infection and immunomodulation properties

Previous in vitro experiments demonstrated the robust bactericidal activity of SQPdFT against *S. aureus* and *E. coli*. Next, we assessed the in vivo anti-infection properties of SQPdFT (Fig. 6a). Initially, we implanted clean, smooth Ti rods (control group) or Ti rods with attached MRSA (Ti, 3DFT, PdFT, SPdFT, and SQPdFT groups) into the femoral medullary cavity of rats and confirmed proper implant placement within the central medullary cavity through micro-CT imaging (Fig. 6b and c). After six weeks, the rats were sacrificed, and the Ti rods were subsequently extracted from their femurs. These rods were then immersed in the bacterial culture medium for 12 h at 37 °C. As depicted in Fig. 6d, the culture media of the control and SQPdFT groups exhibited complete clarity and transparency, whereas the Ti, 3DFT, PdFT, and SPdFT groups displayed varying levels of turbidity, indicating diverse bacterial densities on distinct implant surfaces. Subsequently, we separated the bacteria attached to the Ti rod surface using ultrasound and further confirmed the bacterial load on different implants using CFU quantification. Consistent with previous in vitro findings, bacterial colony counts in the SQPdFT group were significantly lower than those in the Ti, 3DFT, and PdFT groups (Fig. S14). Although SPdFT also exhibited some antibacterial activity, its antibacterial efficacy was not as potent as that of SQPdFT. Additionally, we employed Gram and Hematoxylin-eosin (H&E) staining to assess the infiltration of bacteria and inflammatory cells into the tissue surrounding the implants. As shown in Fig. 6e and g, numerous purple spots were observed in the Ti, 3DFT, and PdFT groups, indicating severe bacterial infection around the implants. In contrast, the bacterial count was significantly reduced in the SPdFT group, and hardly any bacteria were observed in the SQPdFT group. The same was observed for infiltrating inflammatory cells into the tissues surrounding the implants (Fig. 6f). Additionally, H&E staining of the liver, spleen, kidney, heart, and lungs did not reveal any signs of organ toxicity caused by SQPdFT (Fig. S15). Therefore, these results provide

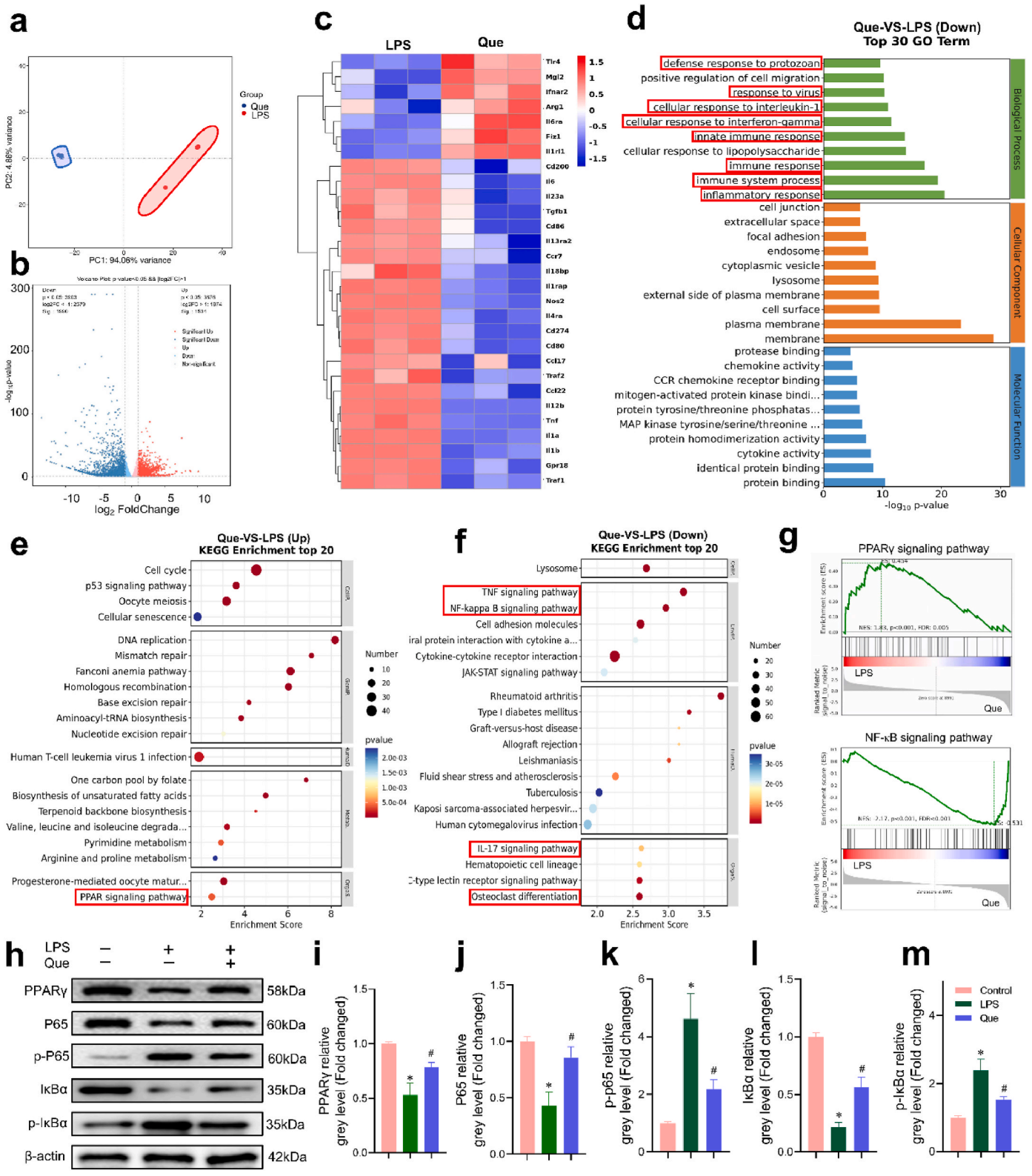

Fig. 4. The mechanism by which Que regulates macrophage polarization homeostasis in vitro. (a) Principal component analysis (PCA) of the LPS group and Que group. (b) Volcano plot of differentially expressed mRNAs. Red indicates upregulation, and blue indicates downregulation. (c) The heatmap shows the expression changes in macrophage polarization-related genes and inflammatory cytokine genes between the LPS group and the Que group. The color bars located to the right of the heatmap depict gene expression levels, where the color red signifies elevated expression, and the color blue signifies reduced expression. (d) Gene ontology (GO) enrichment analysis of the top 30 genes in the LPS group and the Que group. (e) Top 20 upregulated KEGG enriched pathways in the Que group compared with the LPS group. (f) Top 20 downregulated KEGG enriched pathways in the Que group compared with the LPS group. (g) Gene set enrichment analysis (GSEA) of the PPAR and NF-κB pathways. NES, normalized enrichment score. (h–m) Western blot was performed to analyze the PPARγ/NF-κB signaling pathway-related protein expression levels. Data represent mean ± S.D. (n = 3 per group). * indicates a statistical difference compared to the control group ($P < 0.05$) and # indicates a statistical difference compared to the LPS group ($P < 0.05$).

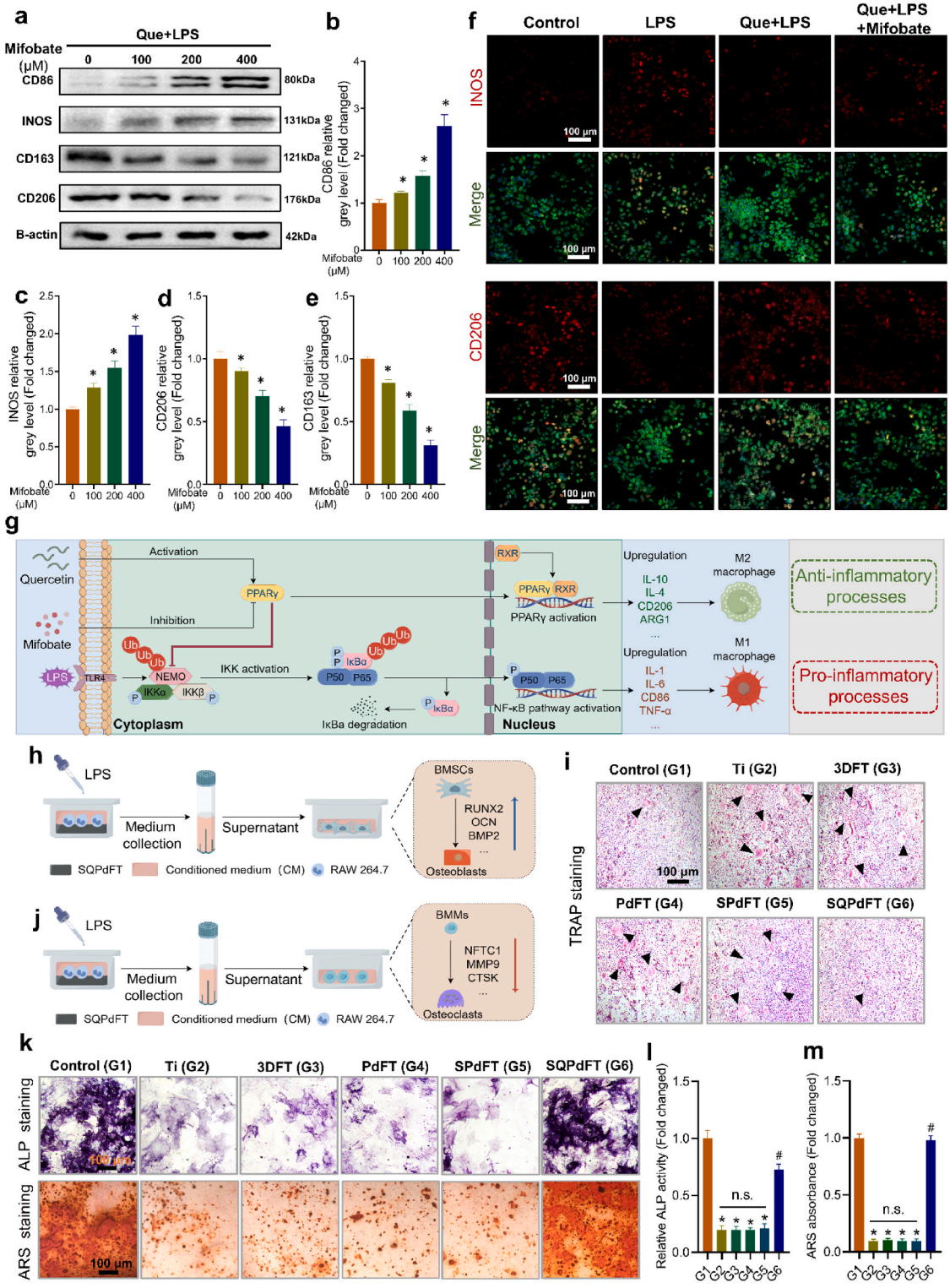

Fig. 5. Experimental validation of the PPARγ/NF-κB signaling pathway activated by Que and bone homeostasis indirectly regulated by SQPdFT in vitro. (a–e) Western blot analysis of macrophage polarization-related proteins. RAW264.7 cells were pretreated with LPS, Que, and various concentrations of Mifobate for 48 h. Data represent mean ± S.D. (n = 3 per group). * indicates a statistical difference compared to the 0 μM group ($P < 0.05$). (f) Images of immunofluorescence staining of iNOS and CD206 in different groups. Scale bar: 100 μm. (g) Diagram of the molecular mechanisms by which Que regulates macrophage polarization via the PPARγ/NF-κB pathway. (h) Schematic of the experimental protocol by which SQPdFT regulates osteoclast differentiation of BMMs in vitro. (i) TRAP staining of BMMs cultured in different induction media. Scale bar: 100 μm. (j) Schematic of the experimental protocol by which SQPdFT regulates osteogenic differentiation of BMSCs in vitro. (k) ALP staining and Alizarin red staining were performed to test the effect of different CM on the osteogenic differentiation of BMSC. Scale bar: 100 μm. (l, m) ALP activity and ARS absorbance detection of BMSCs in the groups of the control, Ti, 3DFT, PdFT, SPdFT, and SQPdFT groups. Data represent mean ± S.D. (n = 3 per group). n.s. indicates no significant, * indicates a statistical difference compared to the control group ($P < 0.05$). # indicates a statistical difference compared to the Ti group ($P < 0.05$).

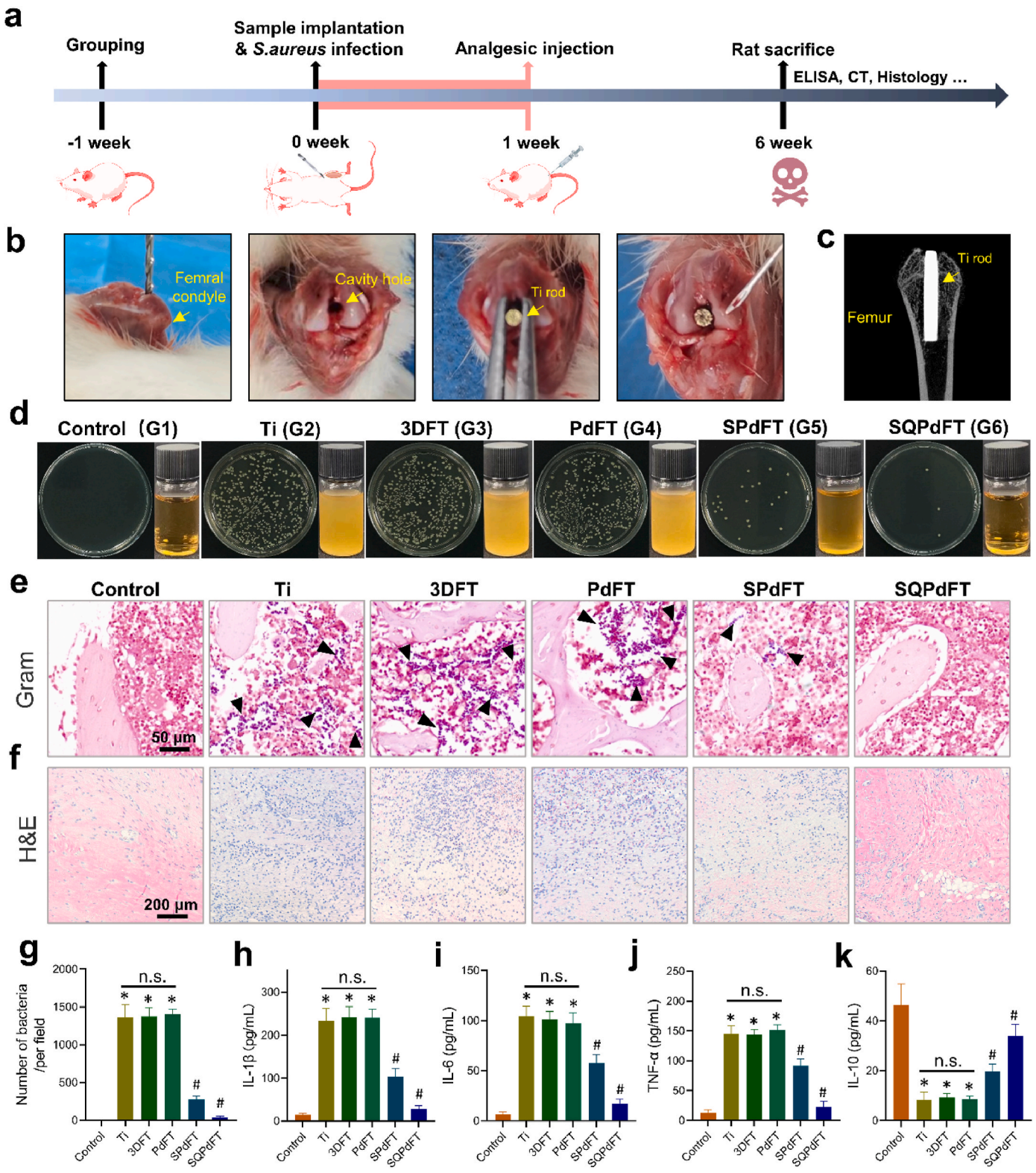

Fig. 6. In vivo antibacterial activity of SQPdFT. (a) Schematic timeline of the in vivo experimental design. (b) The establishment of the rat bone marrow cavity peri-implant infection model. (c) Micro-CT image after implantation of a Ti rod in the distal femur. (d) The bacterial colonies remain on different Ti rod surfaces. (e) Gram staining of the tissue surrounding the Ti rods and the counting of the total number of bacteria per field (n = 5 per group). Scale bar: 200 μm and 50 μm, respectively. (f) H&E staining of the soft tissue surrounding the implants. Scale bar: 200 μm. (g) Quantitative analysis of bacteria per field. Data represent mean ± S. D. (n = 5 per group). (h–k) Quantification of pro-inflammatory factors (IL-1, TNF-α, and IL-6) and the anti-inflammatory factor (IL-10) in serum. Cytokine levels in serum were quantified by ELISA. Data represent mean ± S.D. (n = 5 per group). n.s. indicates no significance, * indicates a statistical difference compared to the control group ($P < 0.05$) and # indicates a statistical difference compared to the Ti group ($P < 0.05$).

compelling evidence that SQPdFT exhibits excellent biosafety and potent antibacterial activity.

Next, we evaluated the impact of SQPdFT on the level of inflammation in peri-implant bone tissue within the same model. As illustrated in Fig. S16, among all bacterial contamination groups (Ti, 3DFT, PdFT, SPdFT, and SQPdFT groups), the thickness of the fibrous layer surrounding SQPdFT was the smallest, followed by SPdFT. Further immunohistochemical results indicated that, compared to other bacterial contamination groups, the SQPdFT group exhibited the lowest expression levels of the inflammatory factors IL-1β, IL-6, and TNF-α. Conversely, IL-10 was expressed at its highest level in the SQPdFT group. ELISA analysis of serum inflammatory cytokine levels showed similar trends (Fig. S17 and Fig. 6h–k). These findings collectively demonstrated that the inflammatory response in the vicinity of SQPdFT was the mildest. Immunofluorescence staining was used to assess the polarization homeostasis of macrophages in the tissues surrounding the implants. As observed in Fig. 7a–e, in the Ti, 3DFT, and SPdFT groups, there was a significant infiltration of M1-type macrophages ($CD86^+$ and $CCR7^+$) and sporadic M2-type macrophages ($CD206^+$ and $ARG1^+$). Conversely, in the SQPdFT group, there was a significant increase in the proportion of M2-type macrophages, accompanied by a reversal of the excessive activation of M1-type macrophages. Notably, SPdFT partially improved the polarization homeostasis of macrophages. The observed disparities in experimental outcomes between the in vitro and in vivo settings can be ascribed to the antibacterial effects of AgNPs against *S. aureus*. These results reconfirm our conclusion that Que can enhance the anti-inflammatory properties of coatings by modulating macrophage polarization phenotypes.

3.8. Osseointegration property assessment

The above results provide robust evidence of the exceptional antibacterial and anti-inflammatory capabilities inherent to AgNPs-Que/PDA hybrid coatings. These characteristics confer advantages to the process of bone-implant interface osseointegration, particularly within the inflammatory microenvironment caused by infections. As expected, Masson's staining revealed that implants in the Ti, 3DFT, and PdFT groups were entirely enveloped by a thick fibrous layer without new bone formation. In sharp contrast, SQPdFT effectively counteracted the inhibitory effects of infection and inflammation on osteogenesis and induced substantial formation of new bone surrounding the implant (Fig. 7f, g). While SPdFT also partially improved bone-implant interface osteointegration, its efficacy was conspicuously inferior to that of SQPdFT. We further examined the inhibitory effect of SQPdFT on osteoclasts in vivo using TRAP staining. Consistent with the in vitro results, the population of osteoclasts within the SQPdFT group was markedly lower than that in the Ti, 3DFT, PdFT, and SPdFT groups (Fig. 7h, i). Additionally, immunohistochemical results substantiated a significant upregulation of the osteoblastic marker OCN and a commensurate downregulation of the osteoclastic marker MMP9 in the SQPdFT group (Fig. 7j–m). These findings highlight the ability of SQPdFT to promote bone formation and inhibit bone resorption by osteoclasts in the presence of inflammation at the implantation site.

To provide a more intuitive assessment of bone integration around the implants, we conducted a three-dimensional reconstruction of micro-CT images for all femoral samples. Consistent with the histological staining results, it is evident that the SQPdFT group exhibited a significantly higher bone volume on the surface of Ti rods compared to the Ti, 3DFT, PdFT, and SPdFT groups, even approaching that of the control group (Fig. 8a). The stability of bone-implant contact is crucial for surgical success and indicates successful bone fusion. Therefore, mechanical push-out tests were conducted to evaluate the maximum anchoring force of the various implants within the femur. The results revealed that the maximum push-out forces of the SQPdFT group (56.33 ± 4.73 N cm) were 2.36-, 2.25-, 2.41-, and 1.47 times higher than those of Ti (23.88 ± 2.08 N cm), 3DFT (25 ± 2.65 N cm), PdFT (23 ± 2.64 N cm), and SPdFT groups (38.33 ± 5.51 N cm), respectively, indicating superior in vivo mechanical stability of the SQPdFT group over the other groups (Fig. 8b, c). Furthermore, we quantitatively analyzed various bone parameters, including trabecular number (Tb. N), trabecular thickness (Tb. Th), trabecular separation (Tb. Sp), bone surface/bone volume ratio (BS/BV), bone mineral density (BMD), bone volume (BV), percentage of bone volume to tissue volume (BV/TV), and connectivity density (Conn.d), as displayed in Fig. 8d–k. All bone parameter indices in the SQPdFT group surpassed those in the Ti, 3DFT, PdFT, and SPdFT groups. These results confirmed that our designed AgNPs-Que/PDA hybrid coating could synergistically enhance bone integration at the bone-implant interface, even in the presence of postoperative infection. However, while our SQPdFT shows great potential in treating peri-implant infections, the current data are derived from rat models. In the future, we will further evaluate biosafety and efficacy in large animal models to provide more convincing data for clinical translation.

4. Conclusions

In summary, we introduce a convenient organic-inorganic hybridization strategy for the preparation of SQPdFT integrated AgNPs and Que for enhanced specific silver bactericidal and excessive inflammatory responses via reprogramming macrophage fate. Once invading planktonic bacteria (*e.g., E. coli*, *S. aureus*) reach the surface of SQPdFT, Que can disrupt the bacterial membrane, facilitating the ingress of AgNPs into the bacterial interior for bactericidal purposes while further inhibiting the formation of biofilms. Notably, Que can also regulate the homeostasis of macrophages via the PPARγ-mediated NF-κB pathway to terminate excessive inflammatory responses. This mechanism rectifies the imbalance between osteoblast differentiation and osteoclast proliferation within the inflammatory microenvironment, thereby expediting osseointegration at the implant-bone interface and providing superior mechanical stability to SQPdFT in the medullary cavity. Therefore, our proposed SQPdFT-based non-antibiotic strategy and macrophage reprogramming strategy establish an optional paradigm to combat peri-implant infections.

Ethics approval and consent to participate

Ethics approval and consent to participate The animal experiments were approved by The Ethics Committees of the First Affiliated Hospital of USTC.

Data availability statement

The data that support the findings of this study are available from the corresponding authors upon reasonable request.

CRediT authorship contribution statement

Ning Yang: Writing – review & editing, Writing – original draft, Project administration, Data curation. **Ting Wu:** Writing – review & editing, Writing – original draft, Project administration. **Meng Li:** Writing – original draft, Project administration, Data curation. **Xianli Hu:** Writing – original draft, Project administration. **Ruixiang Ma:** Software, Project administration. **Wei Jiang:** Project administration. **Zheng Su:** Writing – review & editing, Writing – original draft. **Rong Yang:** Writing – review & editing, Methodology. **Chen Zhu:** Writing – review & editing, Project administration, Methodology, Funding acquisition.

Declaration of competing interest

We declare that we have no financial and personal relationships with other people or organizations that can inappropriately influence our work, there is no professional or other personal interest of any nature or

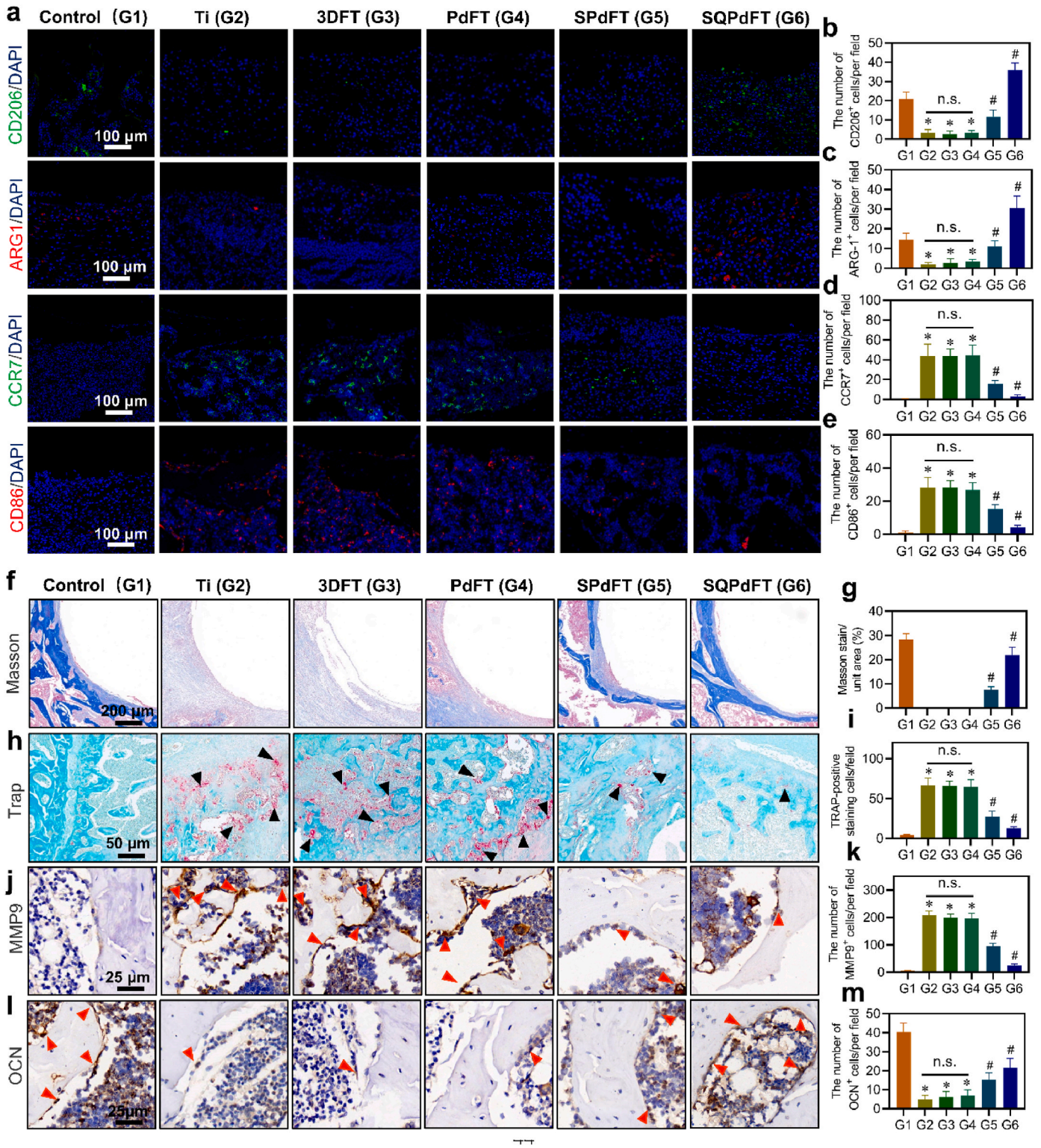

Fig. 7. Histological evaluations of peri-implant macrophage polarization homeostasis and osseointegration. (a) Tissue immunofluorescence staining images of macrophage polarization-related markers (M2 markers: CD206 and ARG1, M1 markers: CCR7 and CD86). Scale bar: 100 μm. (b–e) Quantitative analysis of total numbers of CD206-, ARG1-, CCR7-and CD86 positive cells per field. Data represent mean ± S.D. (n = 5 per group). (f, g) Masson staining of the peri-implant tissue and quantitative analysis of Masson stained area (n = 5 per group). Scale bar: 200 μm. (h, i) TRAP staining of the peri-implant tissue and quantitative analysis of the number of TRAP positive cells per field (n = 5 per group). Scale bar: 50 μm. (j, l) IHC staining of MMP9 and OCN and the positive cells are marked with red arrows. Scale bar: 200 μm and 50 μm, respectively. (k, m) Quantitative analysis of the number of MMP9-positive cells and OCN-positive cells in (j, l). Data represent mean ± S.D. (n = 5 per group). n.s. indicates no significance, * indicates a statistical difference compared to the control group ($P < 0.05$) and # indicates a statistical difference compared to the Ti group ($P < 0.05$).

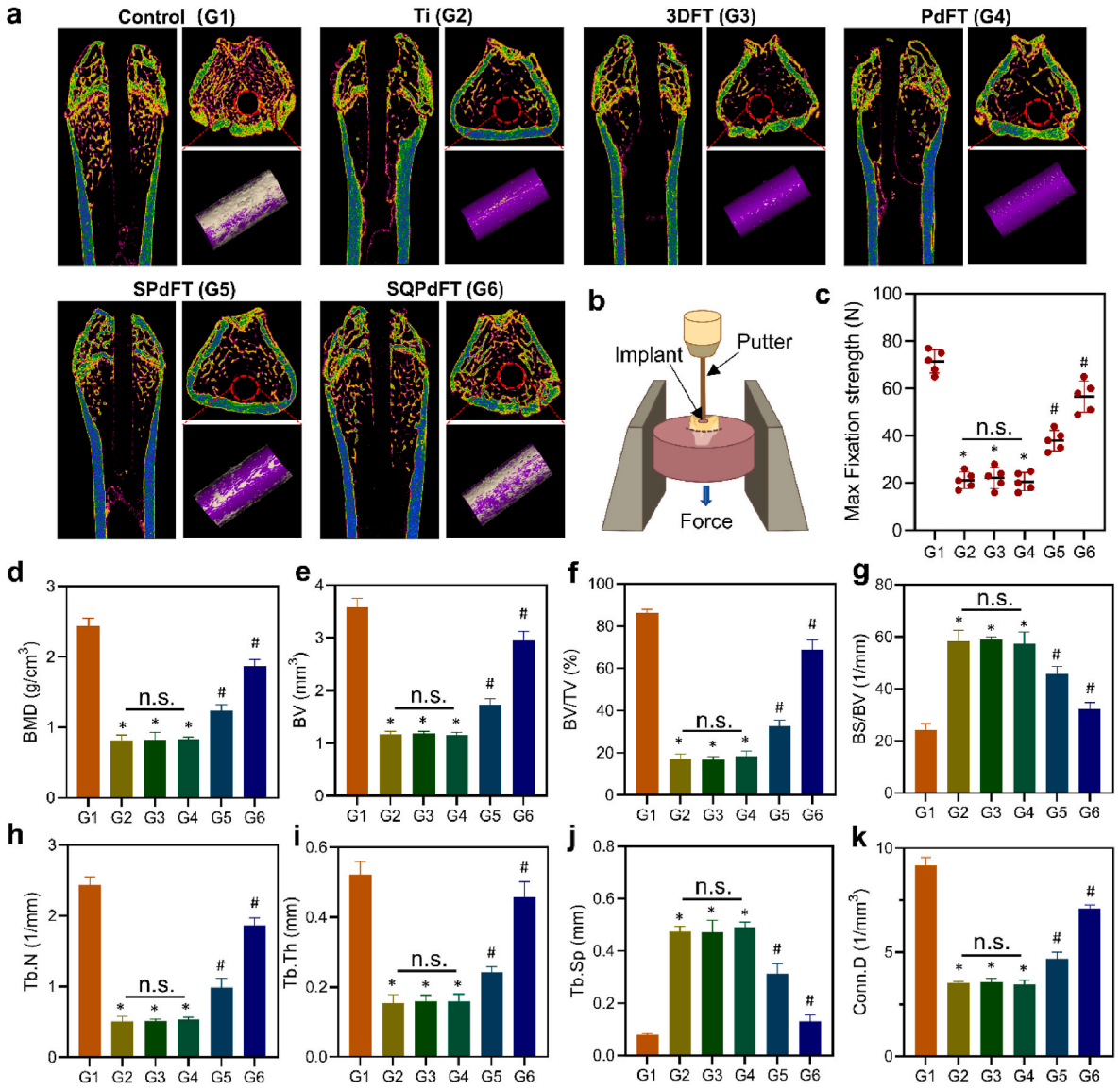

Fig. 8. Micro-CT analyses and mechanical evaluations of peri-implant osseointegration. (a) 3D reconstruction of micro-CT images of the distal femoral and bone-implants interface. (b) Schematic of the biomechanical experiment. (c) Quantitative analysis of max fixation strength in different groups. (d) BMD (g/cm^3). (e) BV (mm^3). (f) BV/TV (%). (g) BS/BV (1/mm). (h) Tb. N (1/mm). (i) Tb.Th (mm). (j) Tb.Sp (mm). (k) Conn.D (1/mm^3). Data represent mean ± S.D. (n = 5 per group). n.s. indicates no significance, * indicates a statistical difference compared to the control group ($P < 0.05$) and # indicates a statistical difference compared to the Ti group ($P < 0.05$).

kind in any product, service and/or company that could be construed as influencing the position presented in, or the review of, the manuscript entitled, "**Silver-Quercetin-loaded honeycomb-like Ti-based interface combats infection-triggered excessive inflammation via specific bactericidal and macrophage reprogramming**".

Acknowledgements

This study was supported by the National Natural Science Foundation of China (NSFC) Projects (82272512, 82102586), the National Key Research and Development Program of China (2022YFA1207300), the Natural Science Foundation of Anhui Province, Distinguishing Youth Project (2108085J40), Anhui Provincial Key Research and Development Program-Clinical Medical Research Translation Specialization (202304295107020020), Anhui Provincial Department of Education Higher Education Research Program (2022AH051251, 2022AH010076), Research Funds of Centre for Leading Medicine and Advanced Technologies of IHM (2023IHM01070, 2023IHM01074), Natural Science Fund for Colleges and Universities in Anhui Province (2023AH053289), Research Fund of Anhui Institute of Translational Medicine (2022zhyx-C32).

Appendix A. Supplementary data

Supplementary data to this article can be found online at https://doi.org/10.1016/j.bioactmat.2024.09.012.

References

[1] Z. Li, Y. He, L.H. Klausen, N. Yan, J. Liu, F. Chen, W. Song, M. Dong, Y. Zhang, Growing vertical aligned mesoporous silica thin film on nanoporous substrate for enhanced degradation, drug delivery and bioactivity, Bioact. Mater. 6 (5) (2021) 1452–1463.

[2] G. Vallés, E. Gil-Garay, L. Munuera, N. Vilaboa, Modulation of the cross-talk between macrophages and osteoblasts by titanium-based particles, Biomaterials 29 (15) (2008) 2326–2335.

[3] Y. Zhang, Z. Cheng, Z. Liu, X. Shen, C. Cai, M. Li, Z. Luo, Functionally tailored metal-organic framework coatings for mediating Ti implant osseointegration, Adv. Sci. 10 (29) (2023) e2303958.

[4] S.D. Puckett, E. Taylor, T. Raimondo, T.J. Webster, The relationship between the nanostructure of titanium surfaces and bacterial attachment, Biomaterials 31 (4) (2010) 706–713.

[5] V.K. Sharma, K.M. Siskova, R. Zboril, J.L. Gardea-Torresdey, Organic-coated silver nanoparticles in biological and environmental conditions: fate, stability and toxicity, Adv. Colloid Interface Sci. 204 (2014) 15–34.

[6] Y. Guo, M. Wang, Q. Liu, G. Liu, S. Wang, J. Li, Recent advances in the medical applications of hemostatic materials, Theranostics 13 (1) (2023) 161–196.

[7] A.C. Burduşel, O. Gherasim, A.M. Grumezescu, L. Mogoantă, A. Ficai, E. Andronescu, Biomedical applications of silver nanoparticles: an up-to-date overview, Nanomaterials 8 (9) (2018).

[8] X. Gao, V.D. Topping, Z. Keltner, R.L. Sprando, J.J. Yourick, Toxicity of nano- and ionic silver to embryonic stem cells: a comparative toxicogenomic study, J. Nanobiotechnol. 15 (1) (2017) 31.

[9] B. Chakraborty, R. Pal, M. Ali, L.M. Singh, D. Shahidur Rahman, S. Kumar Ghosh, M. Sengupta, Immunomodulatory properties of silver nanoparticles contribute to anticancer strategy for murine fibrosarcoma, Cell. Mol. Immunol. 13 (2) (2016) 191–205.

[10] Y. Zheng, A. Gao, J. Bai, Q. Liao, Y. Wu, W. Zhang, M. Guan, L. Tong, D. Geng, X. Zhao, P.K. Chu, H. Wang, A programmed surface on polyetheretherketone for sequentially dictating osteoimmunomodulation and bone regeneration to achieve ameliorative osseointegration under osteoporotic conditions, Bioact. Mater. 14 (2022) 364–376.

[11] Y. Zhao, L. Bai, Y. Zhang, R. Yao, Y. Sun, R. Hang, X. Chen, H. Wang, X. Yao, Y. Xiao, R. Hang, Type I collagen decorated nanoporous network on titanium implant surface promotes osseointegration through mediating immunomodulation, angiogenesis, and osteogenesis, Biomaterials 288 (2022) 121684.

[12] Y.L. Yu, J.J. Wu, C.C. Lin, X. Qin, F.R. Tay, L. Miao, B.L. Tao, Y. Jiao, Elimination of methicillin-resistant Staphylococcus aureus biofilms on titanium implants via photothermally-triggered nitric oxide and immunotherapy for enhanced osseointegration, Mil Med Res 10 (1) (2023) 21.

[13] X. Sheng, C. Li, Z. Wang, Y. Xu, Y. Sun, W. Zhang, H. Liu, J. Wang, Advanced applications of strontium-containing biomaterials in bone tissue engineering, Mater Today Bio. 20 (2023) 100636.

[14] B. Chen, Y. You, A. Ma, Y. Song, J. Jiao, L. Song, E. Shi, X. Zhong, Y. Li, C. Li, Zn-incorporated TiO(2) nanotube surface improves osteogenesis ability through influencing immunomodulatory function of macrophages, Int. J. Nanomed. 15 (2020) 2095–2118.

[15] T. Wang, J. Bai, M. Lu, C. Huang, D. Geng, G. Chen, L. Wang, J. Qi, W. Cui, L. Deng, Engineering immunomodulatory and osteoinductive implant surfaces via mussel adhesion-mediated ion coordination and molecular clicking, Nat. Commun. 13 (1) (2022) 160.

[16] F. Monticolo, E. Palomba, R. De Santis, L. Assentato, V. Triscino, M.C. Langella, V. Lanzotti, M.L. Chiusano, anti-HCoV: a web resource to collect natural compounds against human coronaviruses, Trends Food Sci. Technol. 106 (2020) 1–11.

[17] Y. Wang, M. Zhang, R. Bi, Y. Su, F. Quan, Y. Lin, C. Yue, X. Cui, Q. Zhao, S. Liu, Y. Yang, D. Zhang, Q. Cao, X. Gao, ACSL4 deficiency confers protection against ferroptosis-mediated acute kidney injury, Redox Biol. 51 (2022) 102262.

[18] P. Kuppusamy, M.M. Yusoff, G.P. Maniam, S.J. Ichwan, I. Soundharrajan, N. Govindan, Nutraceuticals as potential therapeutic agents for colon cancer: a review, Acta Pharm. Sin. B 4 (3) (2014) 173–181.

[19] X. Han, T. Xu, Q. Fang, H. Zhang, L. Yue, G. Hu, L. Sun, Quercetin hinders microglial activation to alleviate neurotoxicity via the interplay between NLRP3 inflammasome and mitophagy, Redox Biol. 44 (2021) 102010.

[20] R.Z. Tan, C. Wang, C. Deng, X. Zhong, Y. Yan, Y. Luo, H.Y. Lan, T. He, L. Wang, Quercetin protects against cisplatin-induced acute kidney injury by inhibiting Mincle/Syk/NF-κB signaling maintained macrophage inflammation, Phytother Res. 34 (1) (2020) 139–152.

[21] T. Nalini, S.K. Basha, A.M. Sadiq, V.S. Kumari, In vitro cytocompatibility assessment and antibacterial effects of quercetin encapsulated alginate/chitosan nanoparticle, Int. J. Biol. Macromol. 219 (2022) 304–311.

[22] A. Aygül, İ. Öztürk, F.F. Çilli, Ş. Ermertcan, Quercetin inhibits swarming motility and activates biofilm production of Proteus mirabilis possibly by interacting with central regulators, metabolic status or active pump proteins, Phytomedicine 57 (2019) 65–71.

[23] X. Huang, X. Chen, Q. Chen, Q. Yu, D. Sun, J. Liu, Investigation of functional selenium nanoparticles as potent antimicrobial agents against superbugs, Acta Biomater. 30 (2016) 397–407.

[24] Y. Park, E. Cheong, J.G. Kwak, R. Carpenter, J.H. Shim, J. Lee, Trabecular bone organoid model for studying the regulation of localized bone remodeling, Sci. Adv. 7 (4) (2021).

[25] W. Yang, X. Zhang, K. Wu, X. Liu, Y. Jiao, C. Zhou, Improving cytoactive of endothelial cell by introducing fibronectin to the surface of poly L-Lactic acid fiber mats via dopamine, Mater. Sci. Eng., C 69 (2016) 373–379.

[26] S.B.K. Bourhis, C. Mathe, J.C. Dupin, C. Vieillescazes, Spectroscopic and chromatographic analysis of yellow flavonoidic lakes: quercetin chromophore, Appl. Clay Sci. 53 (2011) 598–607.

[27] H. Liu, W. Li, B. Luo, X. Chen, W. Wen, C. Zhou, Icariin immobilized electrospinning poly(l-lactide) fibrous membranes via polydopamine adhesive coating with enhanced cytocompatibility and osteogenic activity, Mater. Sci. Eng., C 79 (2017) 399–409.

[28] H.G. Luo, C, W. Zheng, F. Dai, X. Wang, Z. Zheng, Facile synthesis of novel size-controlled antibacterial hybrid spheres using silver nanoparticles loaded with polydopamine spheres, RSC Adv. 5 (2015) 13470–13477.

[29] H.C. Gebru, S, Z. Li, X. Wang, X. Pan, J. Liu, K. Guo, Facile pH-dependent synthesis and characterization of catechol stabilized silver nanoparticles for catalytic reduction of 4-nitrophenol, Catal. Lett. 147 (2017) 2134–2143.

[30] C. Wu, Y. Zhang, Y. Zhou, W. Fan, Y. Xiao, A comparative study of mesoporous glass/silk and non-mesoporous glass/silk scaffolds: physiochemistry and in vivo osteogenesis, Acta Biomater. 7 (5) (2011) 2229–2236.

[31] Z. Liu, S. Qu, X. Zheng, X. Xiong, R. Fu, K. Tang, Z. Zhong, J. Weng, Effect of polydopamine on the biomimetic mineralization of mussel-inspired calcium phosphate cement in vitro, Mater. Sci. Eng., C 44 (2014) 44–51.

[32] C.S. Seney, B.M. Gutzman, R.H. Goddard, Correlation of size and surface-enhanced Raman scattering activity of optical and spectroscopic properties for silver nanoparticles, J. Phys. Chem. C 113 (1) (2009) 74–80.

[33] F. Wang, R. Han, G. Liu, H. Chen, T. Ren, H. Yang, Y. Wen, Construction of polydopamine/silver nanoparticles multilayer film for hydrogen peroxide detection, J. Electroanal. Chem. 706 (2013) 102–107.

[34] Q. Han, R. Yang, J. Li, W. Liang, Y. Zhang, M. Dong, F. Besenbacher, C. Wang, Enhancement of biological activities of nanostructured hydrophobic drug species, Nanoscale 4 (6) (2012) 2078–2082.

[35] M. Catauro, F. Papale, F. Bollino, S. Piccolella, S. Marciano, P. Nocera, S. Pacifico, Silica/quercetin sol-gel hybrids as antioxidant dental implant materials, Sci. Technol. Adv. Mater. 16 (3) (2015) 035001.

[36] R. Luo, L. Tang, S. Zhong, Z. Yang, J. Wang, Y. Weng, Q. Tu, C. Jiang, N. Huang, In vitro investigation of enhanced hemocompatibility and endothelial cell proliferation associated with quinone-rich polydopamine coating, ACS Appl. Mater. Interfaces 5 (5) (2013) 1704–1714.

[37] I.I. Niyonshuti, V.R. Krishnamurthi, D. Okyere, L. Song, M. Benamara, X. Tong, Y. Wang, J. Chen, Polydopamine surface coating synergizes the antimicrobial activity of silver nanoparticles, ACS Appl. Mater. Interfaces 12 (36) (2020) 40067–40077.

[38] M. Akter, M.T. Sikder, M.M. Rahman, A. Ullah, K.F.B. Hossain, S. Banik, T. Hosokawa, T. Saito, M. Kurasaki, A systematic review on silver nanoparticles-induced cytotoxicity: physicochemical properties and perspectives, J. Adv. Res. 9 (2018) 1–16.

[39] F. Wang, Z. Chen, Y. Wang, C. Ma, L. Bi, M. Song, G. Jiang, Silver nanoparticles induce apoptosis in HepG2 cells through particle-specific effects on mitochondria, Environ. Sci. Technol. 56 (9) (2022) 5706–5713.

[40] Y.H. Lee, F.Y. Cheng, H.W. Chiu, J.C. Tsai, C.Y. Fang, C.W. Chen, Y.J. Wang, Cytotoxicity, oxidative stress, apoptosis and the autophagic effects of silver nanoparticles in mouse embryonic fibroblasts, Biomaterials 35 (16) (2014) 4706–4715.

[41] K. Xie, Z. Zhou, Y. Guo, L. Wang, G. Li, S. Zhao, X. Liu, J. Li, W. Jiang, S. Wu, Y. Hao, Long-term prevention of bacterial infection and enhanced osteoinductivity of a hybrid coating with selective silver toxicity, Adv. Healthcare Mater. 8 (5) (2019) e1801465.

[42] M. Ai, Z. Du, S. Zhu, H. Geng, X. Zhang, Q. Cai, X. Yang, Composite resin reinforced with silver nanoparticles-laden hydroxyapatite nanowires for dental application, Dent. Mater. 33 (1) (2017) 12–22.

[43] W. Bian, S. Xiao, L. Yang, J. Chen, S. Deng, Quercetin promotes bone marrow mesenchymal stem cell proliferation and osteogenic differentiation through the H19/miR-625-5p axis to activate the Wnt/β-catenin pathway, BMC Complement Med Ther. 21 (1) (2021) 243.

[44] C.F. Tsai, G.W. Chen, Y.C. Chen, C.K. Shen, D.Y. Lu, L.Y. Yang, J.H. Chen, W.L. Yeh, Regulatory effects of quercetin on M1/M2 macrophage polarization and oxidative/antioxidative balance, Nutrients 14 (1) (2021).

[45] N. Liu, H. Wang, Z. Fu, C. Zhang, W. Hui, J. Wu, Y. Zhang, S. Zhang, Quercetin-coating promotes osteogenic differentiation, osseointegration and anti-inflammatory properties of nano-topographic modificated 3D-printed Ti6Al4V implant, Front. Bioeng. Biotechnol. 10 (2022) 933135.

[46] M. Muller, N.D. Merrett, Pyocyanin production by Pseudomonas aeruginosa confers resistance to ionic silver, Antimicrob. Agents Chemother. 58 (9) (2014) 5492–5499.

[47] D. Panáček, L. Hochvaldová, A. Bakandritsos, T. Malina, M. Langer, J. Belza, J. Martincová, R. Večeřová, P. Lazar, K. Poláková, J. Kolařík, L. Válková, M. Kolář, M. Otyepka, A. Panáček, R. Zbořil, Silver covalently bound to cyanographene overcomes bacterial resistance to silver nanoparticles and antibiotics, Adv. Sci. 8 (12) (2021) 2003090.

[48] A. Panáček, L. Kvítek, M. Smékalová, R. Večeřová, M. Kolář, M. Röderová, F. Dyčka, M. Šebela, R. Prucek, O. Tomanec, R. Zbořil, Bacterial resistance to silver nanoparticles and how to overcome it, Nat. Nanotechnol. 13 (1) (2018) 65–71.

[49] M. Muller, Bacterial silver resistance gained by cooperative interspecies redox behavior, Antimicrob. Agents Chemother. 62 (8) (2018).

[50] J. Rodríguez-Baño, B. Gutiérrez-Gutiérrez, I. Machuca, A. Pascual, Treatment of infections caused by extended-spectrum-beta-lactamase-, AmpC-, and carbapenemase-producing enterobacteriaceae, Clin. Microbiol. Rev. 31 (2) (2018).

[51] G.G. Rao, J. Li, S.M. Garonzik, R.L. Nation, A. Forrest, Assessment and modelling of antibacterial combination regimens, Clin. Microbiol. Infect. 24 (7) (2018) 689–696.

[52] S.S. Kanj, M. Bassetti, P. Kiratisin, C. Rodrigues, M.V. Villegas, Y. Yu, D. van Duin, Clinical data from studies involving novel antibiotics to treat multidrug-resistant Gram-negative bacterial infections, Int. J. Antimicrob. Agents 60 (3) (2022) 106633.

[53] S. Wang, J. Yao, B. Zhou, J. Yang, M.T. Chaudry, M. Wang, F. Xiao, Y. Li, W. Yin, Bacteriostatic effect of quercetin as an antibiotic alternative in vivo and its antibacterial mechanism in vitro, J. Food Protect. 81 (1) (2018) 68–78.
[54] X. Yang, W. Zhang, Z. Zhao, N. Li, Z. Mou, D. Sun, Y. Cai, W. Wang, Y. Lin, Quercetin loading CdSe/ZnS nanoparticles as efficient antibacterial and anticancer materials, J. Inorg. Biochem. 167 (2017) 36–48.
[55] A. Pal, A. Tripathi, Demonstration of bactericidal and synergistic activity of quercetin with meropenem among pathogenic carbapenem resistant Escherichia coli and Klebsiella pneumoniae, Microb. Pathog. 143 (2020) 104120.
[56] Y. Zhao, M. Chen, Z. Zhao, S. Yu, The antibiotic activity and mechanisms of sugarcane (Saccharum officinarum L.) bagasse extract against food-borne pathogens, Food Chem. 185 (2015) 112–118.
[57] M. Li, J. Bai, H. Tao, L. Hao, W. Yin, X. Ren, A. Gao, N. Li, M. Wang, S. Fang, Y. Xu, L. Chen, H. Yang, H. Wang, G. Pan, D. Geng, Rational integration of defense and repair synergy on PEEK osteoimplants via biomimetic peptide clicking strategy, Bioact. Mater. 8 (2022) 309–324.
[58] C.R. Arciola, D. Campoccia, L. Montanaro, Implant infections: adhesion, biofilm formation and immune evasion, Nat. Rev. Microbiol. 16 (7) (2018) 397–409.
[59] O. Ciofu, C. Moser, P. Jensen, N. Høiby, Tolerance and resistance of microbial biofilms, Nat. Rev. Microbiol. 20 (10) (2022) 621–635.
[60] S. Wu, J. Xu, L. Zou, S. Luo, R. Yao, B. Zheng, G. Liang, D. Wu, Y. Li, Long-lasting renewable antibacterial porous polymeric coatings enable titanium biomaterials to prevent and treat peri-implant infection, Nat. Commun. 12 (1) (2021) 3303.
[61] J.H. Fu, H.L. Wang, Breaking the wave of peri-implantitis, Periodontol. 2000 84 (1) (2020) 145–160.
[62] X.B. Duan, T.X. Wu, Y.C. Guo, X.D. Zhou, Y.L. Lei, X. Xu, A.C. Mo, Y.Y. Wang, Q. Yuan, Marginal bone loss around non-submerged implants is associated with salivary microbiome during bone healing, Int. J. Oral Sci. 9 (2) (2017) 95–103.
[63] J.O. Abaricia, A.H. Shah, M. Chaubal, K.M. Hotchkiss, R. Olivares-Navarrete, Wnt signaling modulates macrophage polarization and is regulated by biomaterial surface properties, Biomaterials 243 (2020) 119920.
[64] X. Zhu, B. Huang, F. Zhao, J. Lian, L. He, Y. Zhang, L. Ji, J. Zhang, X. Yan, T. Zeng, C. Ma, Y. Liang, C. Zhang, J. Lin, p38-mediated FOXN3 phosphorylation modulates lung inflammation and injury through the NF-κB signaling pathway, Nucleic Acids Res. 51 (5) (2023) 2195–2214.
[65] S.C. Sun, The non-canonical NF-κB pathway in immunity and inflammation, Nat. Rev. Immunol. 17 (9) (2017) 545–558.
[66] Z. Shao, B. Wang, Y. Shi, C. Xie, C. Huang, B. Chen, H. Zhang, G. Zeng, H. Liang, Y. Wu, Y. Zhou, N. Tian, A. Wu, W. Gao, X. Wang, X. Zhang, Senolytic agent Quercetin ameliorates intervertebral disc degeneration via the Nrf2/NF-κB axis, Osteoarthritis Cartilage 29 (3) (2021) 413–422.
[67] B. Gross, M. Pawlak, P. Lefebvre, B. Staels, PPARs in obesity-induced T2DM, dyslipidaemia and NAFLD, Nat. Rev. Endocrinol. 13 (1) (2017) 36–49.
[68] A. Christofides, E. Konstantinidou, C. Jani, V.A. Boussiotis, The role of peroxisome proliferator-activated receptors (PPAR) in immune responses, Metabolism 114 (2021) 154338.
[69] S.P. Bapat, C. Whitty, C.T. Mowery, Y. Liang, A. Yoo, Z. Jiang, M.C. Peters, L. J. Zhang, I. Vogel, C. Zhou, V.Q. Nguyen, Z. Li, C. Chang, W.S. Zhu, A.T. Hastie, H. He, X. Ren, W. Qiu, S.G. Gayer, C. Liu, E.J. Choi, M. Fassett, J.N. Cohen, J. L. Sturgill, L.E. Crotty Alexander, J.M. Suh, C. Liddle, A.R. Atkins, R.T. Yu, M. Downes, S. Liu, B.S. Nikolajczyk, I.K. Lee, E. Guttman-Yassky, K.M. Ansel, P. G. Woodruff, J.V. Fahy, D. Sheppard, R.L. Gallo, C.J. Ye, R.M. Evans, Y. Zheng, A. Marson, Obesity alters pathology and treatment response in inflammatory disease, Nature 604 (7905) (2022) 337–342.
[70] C.C. Yang, C.H. Wu, T.C. Lin, Y.N. Cheng, C.S. Chang, K.T. Lee, P.J. Tsai, Y.S. Tsai, Inhibitory effect of PPARγ on NLRP3 inflammasome activation, Theranostics 11 (5) (2021) 2424–2441.
[71] Y. Hou, F. Moreau, K. Chadee, PPARγ is an E3 ligase that induces the degradation of NFκB/p65, Nat. Commun. 3 (2012) 1300.
[72] M. Xu, Y. Li, X. Wang, Q. Zhang, L. Wang, X. Zhang, W. Cui, X. Han, N. Ma, H. Li, H. Fang, S. Tang, J. Li, Z. Liu, H. Yang, X. Jia, Role of hepatocyte- and macrophage-specific PPARγ in hepatotoxicity induced by diethylhexyl phthalate in mice, Environ. Health Perspect. 130 (1) (2022) 17005.
[73] H.F. Zhou, C. Yang, J.Y. Li, Y.Y. He, Y. Huang, R.J. Qin, Q.L. Zhou, F. Sun, D.S. Hu, J. Yang, Quercetin serves as the major component of Xiang-lian Pill to ameliorate ulcerative colitis via tipping the balance of STAT1/PPARγ and dictating the alternative activation of macrophage, J. Ethnopharmacol. 313 (2023) 116557.
[74] R. Zhong, L. Miao, H. Zhang, L. Tan, Y. Zhao, Y. Tu, M. Angel Prieto, J. Simal-Gandara, L. Chen, C. He, H. Cao, Anti-inflammatory activity of flavonols via inhibiting MAPK and NF-κB signaling pathways in RAW264.7 macrophages, Curr. Res. Food Sci. 5 (2022) 1176–1184.
[75] S.H. Lim, H.S. Lee, H.K. Han, C.I. Choi, Saikosaponin A and D inhibit adipogenesis via the AMPK and MAPK signaling pathways in 3T3-L1 adipocytes, Int. J. Mol. Sci. 22 (21) (2021).
[76] E. Papageorgiou, N. Pitulis, P. Msaouel, P. Lembessis, M. Koutsilieris, The non-genomic crosstalk between PPAR-gamma ligands and ERK1/2 in cancer cell lines, Expert Opin. Ther. Targets 11 (8) (2007) 1071–1085.